2018

Effect of Uniaxial Tension on the Microstructure and Texture of High Mn Steel

Sudipta Pramanik
University of Wollongong, sp345@uowmail.edu.au

Azdiar Adil Gazder
University of Wollongong, azdiar@uow.edu.au

Ahmed A. Saleh
University of Wollongong, asaleh@uow.edu.au

Dagoberto Brandao Santos
Federal University of Minas Gerais, dsantos@demet.ufmg.br

Elena V. Pereloma
University of Wollongong, elenap@uow.edu.au

Effect of Uniaxial Tension on the Microstructure and Texture of High Mn Steel

Abstract

Cold-rolled to 42% thickness reduction and annealed at 500, 625, and 700 C, an Fe-17Mn-3Al-2Si-1Ni-0.06C wt% steel is subjected to uniaxial tension and characterized via digital image correlation and electron back-scattering diffraction. The cold-rolled and 500 C samples return similar microstructures comprising predominantly α0-martensite and remnant e-martensite fractions and a trace fraction of untransformed austenite (γ) before and after uniaxial tension. For the 625 and 700 C samples, uniaxial tension results in the transformation of the initially reverted and recrystallized γ into e and α0-martensite via strain localization. The γ shows the formation of h111iγ, h100iγ double-fiber texture, whereas the e and α0-martensite show the development of the {hkil}e and h110iα0 || ND fibers, respectively. 1012gh1011ie extension twinning is also observed in e-martensite upon uniaxial tension. The cold-rolled sample exhibits a mixed brittle and ductile fracture mode. The fracture of the 500 C sample is similar to that of the cold-rolled sample, whereas the 625 and 700 C samples display a ductile fracture mode.

Disciplines

Engineering | Science and Technology Studies

Publication Details

Pramanik, S., Gazder, A. A., Saleh, A. A., Santos, D. B. & Pereloma, E. V. (2018). Effect of Uniaxial Tension on the Microstructure and Texture of High Mn Steel. Advanced Engineering Materials, 20 (11), 1800258-1-1800258-12.

Effect of uniaxial tension on the microstructure and texture of high Mn steel

Sudipta Pramanik[1], Azdiar A. Gazder[2], Ahmed A. Saleh[1], Dagoberto B. Santos[3], Elena V. Pereloma[1,2]

[1]School of Mechanical, Materials, Mechatronic and Biomedical Engineering, University of Wollongong, New South Wales 2522, Australia

[2]Electron Microscopy Centre, University of Wollongong, New South Wales 2500, Australia

[3]Department of Metallurgical and Materials Engineering, Universidade Federal de Minas Gerais, Belo Horizonte, MG 30901-270, Brazil

Abstract

Cold-rolled to 42% thickness reduction and annealed at 500, 625 and 700 °C, an Fe-17Mn-3Al-2Si-1Ni-0.06C wt.% steel was subjected to uniaxial tension and characterised via digital image correlation and electron back-scattering diffraction. The cold-rolled and 500 °C annealed samples returned similar microstructures comprising predominantly α′-martensite and remnant ε-martensite fractions and a trace fraction of untransformed austenite (γ) before and after tension. For the 625 and 700 °C annealed samples, uniaxial tension resulted in the transformation of the initially reverted and recrystallised γ into ε and α′-martensite via strain localisation. γ showed the formation of $\langle 111\rangle_{\gamma}$, $\langle 100\rangle_{\gamma}$ double-fibre texture whereas ε and α′-martensite showed the development of the $\{hkil\}_{\varepsilon}$ and $\langle 110\rangle_{\alpha'}$ || ND fibres, respectively. $\{10\bar{1}2\}\langle\bar{1}011\rangle_{\varepsilon}$ extension twining was also observed in ε-martensite upon uniaxial tension. The cold-rolled sample exhibited a mixed brittle and ductile fracture mode. The fracture of the 500 °C annealed sample was similar to that of the cold-rolled sample, whereas the 625 and 700 °C annealed samples displayed a ductile fracture mode.

Keywords: high Mn steel; phase transformation; electron back-scattering diffraction (EBSD); digital image correlation (DIC); mechanical properties

1. Introduction

Metastable high manganese (Mn) transformation and/or twinning induced plasticity (TRIP-TWIP) steels are suitable for automotive applications because of their superior crash resistance properties which result in enhanced passenger safety. In addition, their high ultimate tensile strengths (UTS) allows vehicle mass reduction due to the decreased thickness of parts used, leading to a higher fuel efficiency [1]. Although high Mn steels exhibit a very attractive combination of mechanical properties, their usage is limited due to their high cost and liquid metal embrittlement during joining of zinc-coated sheets [1].

The supplementary Table 1 is a summary of literature-based tensile properties and processing history of high Mn steels. It clearly shows that for steels that were processed by solution treatment and hot rolling, further processing by cold rolling and annealing leads to a higher UTS and total elongations on account of grain refinement. Furthermore, an initially dual-phase Fe-23.4Mn-0.03Al-0.06Si-0.08C (in wt.% from here on) steel with approximately equal area fractions of reverted and recrystallised face-centred cubic (fcc) austenite (γ) and hexagonal closed packed (hcp) ε-martensite had 844-875 MPa UTS [2]. On the other hand, the same steel with a fully recrystallised initial γ microstructure displayed a UTS of only 792 MPa. It followed that the reverted microstructures possessed higher UTS than their fully recrystallised counterparts. Consequently, the present study assesses the tensile properties of a metastable Fe-17Mn-3Al-2Si-1Ni-0.06C steel in its cold-rolled, reverted and fully recrystallised conditions via digital image correlation (DIC) and electron back-scattering diffraction (EBSD).

Uniaxial tension complemented with DIC is a viable tool to investigate the deformation accommodation and/or phase transformation behaviour in Mn steels. In single crystal Fe-12.3Mn-1.3C Hadfield steel, DIC revealed that twinning during uniaxial tension was accompanied by large strain localisations; by narrow bands of high axial strain along the gauge length. In polycrystalline TWIP and medium Mn steels, DIC enabled the characterisation

of Portevin-LeChátelier (PLC) band formation [3-9]. DIC coupled with synchrotron X-ray diffraction investigation during the closed die forming of a T-shape panel of an Fe-10Mn-0.5C-1.5Al-0.2Si steel showed the dependence of phase transformation behaviour on strain path [10]. It was observed that regions of the T-shape panel subjected to uniaxial tension and plane strain tension showed the highest and lowest volume fraction of retained γ, respectively, due to the transformation of γ to α′-martensite [10].

DIC studies on metastable austenitic stainless, dual-phase, TRIP and TWIP-TRIP steels have focused on the phase transformation behaviour during tensile testing [11-13]. A DIC study on the metastable austenitic stainless steel comprising a single-phase, γ starting microstructure showed the development of heterogeneously distributed regions of high axial and shear strains along the gauge length corresponding to the localised areas undergoing a phase transformation to body-centred cubic (bcc) α′-martensite [14].

A DIC and magnetic measurement investigation on a dual-phase Fe-10.3Mn-2.9Al-0.2C steel comprising bcc ferrite (α)+γ as the starting microstructure showed the localised phase transformation of γ to α′-martensite during the propagation of PLC bands [15]. Similar observations were also reported for a dual-phase α+γ Fe-5Mn-2.5Al-0.2C steel [16]. μ-DIC studies on α + α′-martensite dual-phase steels [17-19] showed strain localisation in an α grain constrained between two α′-martensite grains. During further loading, a strong strain heterogeneity developed in the microstructure. The μ-DIC investigation also showed the nucleation of micro-cracks at α grain boundaries orientated at ~45° to the tensile axis and also at α/α′-martensite interphase boundaries. In that study, the damage resistance of α/α′-martensite interphase boundaries was observed to increase with the decrease in the α′-martensite grain size. The DIC studies on TRIP-aided multi-phase steels showed a large strain partitioning effect in the softer α phase compared to the harder bainitic α and α′-martensite phases [20]. The DIC studies on an Fe-25Mn-12.1Cr-0.33C-0.42N TWIP steel showed a homogenous strain distribution across the gauge length until UTS [21]. However, strain

localisation due to shear bands at ~54° to the tensile axis was noted after UTS. Strain localisation associated with the initiation and the propagation of PLC bands was also observed in high Mn TWIP steels subjected to uniaxial tension [22-25].

In one of the studies on TRIP-TWIP steels, Eskandari et al. [12] used a combination of EBSD and DIC to characterise an Fe-21Mn-2.5Si-1.6Al-0.11C steel subjected to room temperature uniaxial tension at 0.001 s^{-1} strain rate. At the onset of micro-yielding (~0.02 true strain), the single-phase γ microstructure manifested transformation to deformation-induced ε-martensite. Higher tensile strains resulted in the further phase transformation to α′-martensite; along with a concomitant increase in strain inhomogeneity across the gauge length. Thereafter, the fracture was ascribed to the nucleation and coalescence of cracks at the intersection of α′-martensite plates.

Tensile testing at 0.003 s^{-1} strain rate resulted in a greater strain localisation which was attributed to more pronounced phase transformation to ε-martensite compared to uniaxial tension at 0.001 s^{-1} strain rate [11]. Furthermore, uniaxial tension at 180 and 300 °C, 0.001 s^{-1} strain rate revealed the preference for γ-twinning over phase transformation to ε and α′-martensite [11] along with the early onset of strain localisation in axial strain along the gauge length.

To-date, limited studies are conducted to elucidate the strain localisation using DIC in phase transforming high Mn steels subjected to uniaxial tension [10-12]. Although tensile testing was performed on a steel of similar composition [13, 26], it was undertaken without DIC. Furthermore, the microstructural characterisation via EBSD before and after tension was also missing. The present investigation explored the effect of uniaxial tension on a high Mn steel with different initial microstructures through not only characterisation of strain along the gauge length, but by a detailed comparison of the microstructure and texture before and after the tension test. This revealed the dominant deformation mechanisms and the evolution of texture components for each condition. The microstructural characterisation also exposed

extension twins in ε-martensite which formed upon uniaxial tension. Furthermore, the effect of initial microstructure on the fracture behaviour was studied and related to the observed ductility after tension.

2. Experimental procedure

An Fe-17Mn-3Al-2Si-1Ni-0.06C steel was slab cast and reheated at 1100 °C for 7200 s. The slab was then hot-rolled at 1100 °C to 52.5% thickness reduction in 4 passes and subsequently cold-rolled to 42% thickness reduction in 11 passes.

Dog-bone tensile samples of 35 mm gauge length, 6 mm width and 2 mm thickness were wire-cut from the centre of the cold-rolled sheet parallel to the rolling (RD), transverse (TD) and normal (ND) directions, respectively. In addition, rectangular samples of 10 × 7 × ~5 mm^3 were cut parallel to the RD, TD and ND. Both dog-bone and rectangular samples were isochronally annealed at 500, 625 and 700 °C for 300 s and immediately water quenched.

The dog-bone tensile samples were coated with white and black paints to create a uniform background and speckle pattern, respectively. Following this, uniaxial tension was undertaken on a 100 kN Instron 1341 universal testing machine operating in speed control mode at a starting strain rate of 0.001 s^{-1} with an initial crosshead speed of 0.035 mms^{-1}. DIC data of the evolution in axial, transverse and shear strains along the entire gauge length was recorded with a resolution of 5 megapixels by two charge-coupled device cameras manufactured by Dantec Dynamics and operating at 10 frames per second with an exposure time between 20-50 milliseconds. The shear strain was defined as the strain in the XY (transverse-axial) plane. The post-processing of the DIC data was undertaken within the Instra-4D software suite.

For the characterisation of microstructure before tensile testing, 3 mm diameter discs were punched out from the thin RD-ND plane slices. The discs were ground to ~60-70 μm thickness using 1200 and 2400 grit paper. Twin-jet electro-polishing of the discs were conducted using

a Struers Tenupol-5 with a solution of 90% methanol and 10% perchloric acid in order to produce electron transparent foils under the operating conditions of 30 V, ~150 mA at -25 °C. The RD-ND planes of the rectangular undeformed (10 × 7 × ~5 mm^3) and deformed (15 × 6 × 2 mm^3) samples taken from the parallel gauge length of the fractured dog-bone samples were ground to 2400 grit and electro-polished in a Struers LectroPol-5 operating at 50 V for 90 s with a solution of 330 ml methanol, 330 ml butoxyethanol and 40 ml perchloric acid.

Here it should be noted that the electro-polished surfaces of the rectangular undeformed samples were used to gather texture data whereas those of the rectangular deformed samples were used for both, microstructure and texture characterisation.

EBSD was undertaken on a JEOL JSM-7001F field emission gun-scanning electron microscope (FEG-SEM) operating at 15 kV accelerating voltage, ~6.5 nA probe current and at working distances of 12 mm (for the electron transparent thin foils) and 15 mm (for the rectangular samples). A relatively finer step sizes of 0.03 and 0.1 μm and coarser step sizes of 1.0 and 2.5 μm were employed for microstructure and texture characterisation, respectively.

Fractography on the TD-ND plane of the dog-bone samples was undertaken on the same FEG-SEM by collecting secondary electron images at 15 kV, ~6.5 nA and 25 mm working distance.

2.1 EBSD data post-processing

The EBSD maps for microstructural characterisation were post-processed using the Oxford Instruments (OI) Channel-5 software suite. The EBSD maps were cleaned by the removal of wild spikes, cyclic extrapolation of zero solutions to five neighbours and thresholding the band contrast to delineate the unindexed regions. In this study, the phases were superimposed on the band contrast map such that the red, green, blue and white colours denote the γ, ε, α′-martensite phases and unindexed regions, respectively. For all calculations, misorientations between 2°-15° and greater than 15° were classified as low (LAGBs) and high (HAGBs) -angle grain boundaries, respectively. For the purposes of illustration, the EBSD

maps after tension comprise LAGBs between 5°-15°. γ-twin boundaries were defined as Σ3 = 60°/$\langle 111 \rangle_\gamma$ with a maximum deviation (Δθ) of 6.03° as per the Palumbo-Aust criterion (Δθ ≤15° $\Sigma^{-5/6}$) [27]. $\{10\bar{1}2\}\langle\bar{1}011\rangle_\varepsilon$ extension twins in ε-martensite were defined as ~86°/ $\langle 1\bar{2}10 \rangle_\varepsilon$ with a Δθ of 5° [28]. The $\{111\}_\gamma$, $\{100\}_\gamma$, $\{0001\}_\varepsilon$ and $\{110\}_{\alpha'}$ pole figures were plotted using JTEX [29] after exporting the orientation data from OI Channel-5.

3. Results and discussion

3.1 Microstructural changes before and after tension

The cold-rolled microstructure comprised elongated and fragmented α′-martensite as the dominant phase with remnant ε-martensite and a trace fraction of untransformed γ (Fig. 1a). Similar results were reported for cold-rolled high Mn steels [30-32]. Gazder et al. [31, 32] showed the presence of stacking faults in ε-martensite by correlative transmission Kikuchi diffraction/transmission electron microscopy and suggested the deformation accommodation in ε-martensite. Using in-situ tensile testing accompanied by neutron diffraction, Saleh et al. [33] demonstrated ε-martensite to undertake compressive strains, which also indicated that ε-martensite accommodates deformation. During the plane strain compression of the present steel to 20% thickness reduction, the transformation of γ to deformation-induced ε and α′-martensite was observed without the formation of deformation-induced twins in γ [34]. The microstructure of the 500 °C sample indicated that the reversion of ε and α′-martensite phases back to γ was underway (Fig. 1b). Annealing at 625 °C produced a microstructure comprising an approximately even mixture of α′-martensite and reverted/recrystallising γ (Fig. 1c). The α′-martensite either neighbours the γ phase or was present as remnants within the reverted γ grains. Annealing at 700 °C showed that γ recrystallisation is complete and that γ grains contained annealing twins as well as plate-like ε-martensite and/or lenticular/plate-like α′-martensite (Fig. 1d). In this case, the ε and α′-martensite are produced upon quenching after annealing.

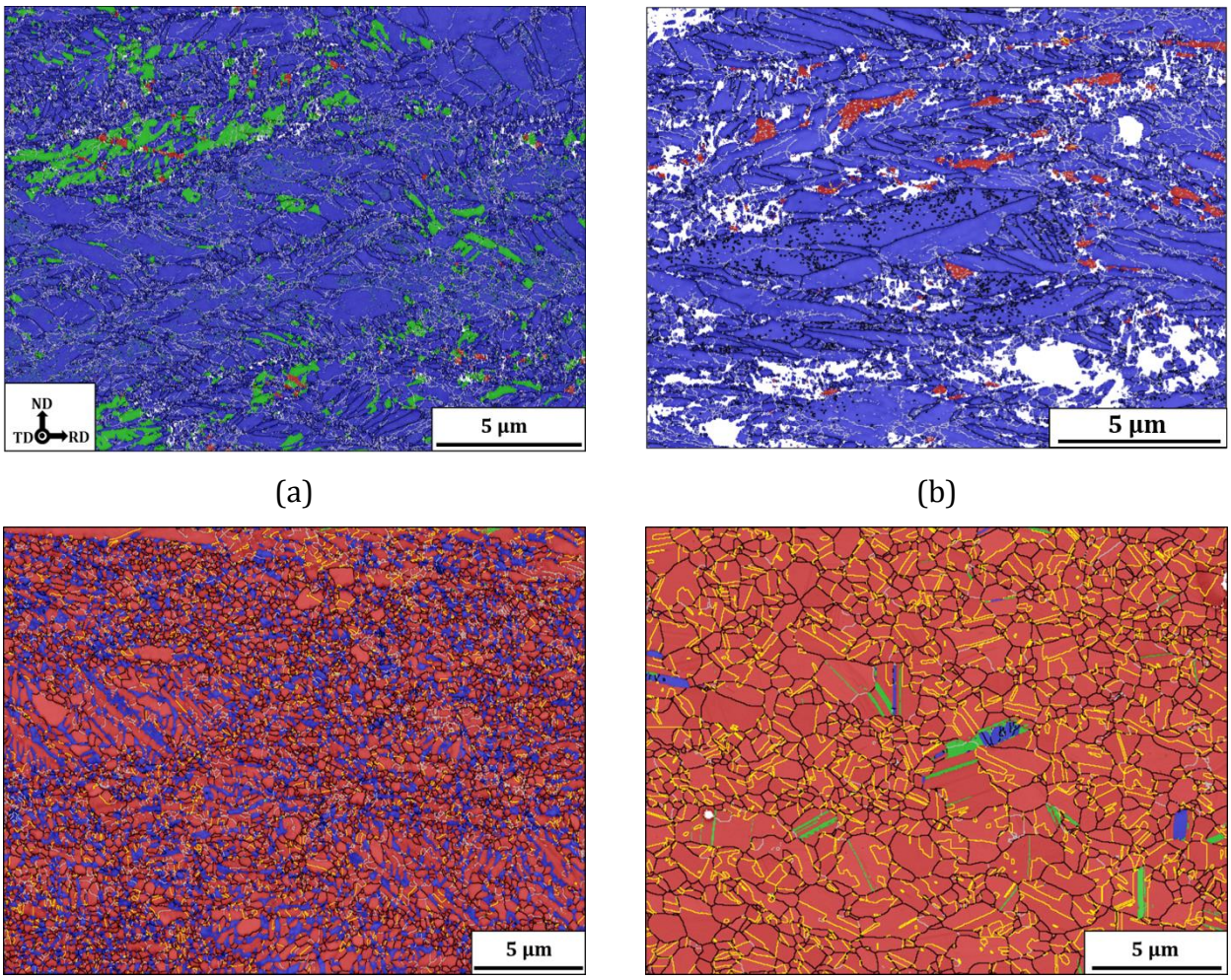

(a) (b)

(c) (d)

Figure 1: Superimposed band contrast and phase maps after (a) cold rolling and annealing at (b) 500 °C, (c) 625 °C and (d) 700 °C. Red = γ, green = ε-martensite, blue = α′-martensite, white = unindexed regions, silver = LAGBs, black = HAGBs and yellow = γ twin boundaries.

The cold-rolled and 500, 625 and 700 °C sample microstructures after tensile testing to fracture at true strains of 0.02, 0.02, 0.23 and 0.31, respectively, are displayed in Fig. 2. Figs. 2a and 2b are similar in terms of morphologies and phase fractions to their undeformed counterparts in Figs. 1a and 1b. Alternatively, the most notable changes in the microstructure upon uniaxial tension were seen in Figs. 2c and 2d (compare with Figs. 1c and 1d).

Tensile testing of the 625 °C sample resulted in the phase transformation of the previously reverted/recrystallising γ into fine deformation-induced ε and α′-martensite (compare Figs. 1c and 2c). On the other hand, while the tensile testing of the 700 °C sample also leads to a

predominant fraction of α′-martensite, the sizes of these grains are larger (compare Figs. 2c and 2d). The variation in morphology of the deformation-induced α′-martensite could be ascribed to the size differences of the γ grains before tension. An ε-martensite grain containing $\{10\bar{1}2\}\langle\bar{1}011\rangle_{\varepsilon}$ extension twins is shown in Fig. 2d (inset). It has to be stated here that for the nucleation of $\{10\bar{1}2\}\langle\bar{1}011\rangle_{\varepsilon}$ extension twins, slip on the basal and pyramidal planes in ε-martensite must be initiated [35]. Thus, the basal and pyramidal planes in ε-martensite also accommodate deformation.

There are also notable differences in the spread of the remnant γ phase between Figs. 2c and 2d; which indicated that the greater fraction of γ grains transform to α′-martensite on account of the higher strain to fracture for the 700 °C sample (i.e. – true strains of 0.23 and 0.31, respectively).

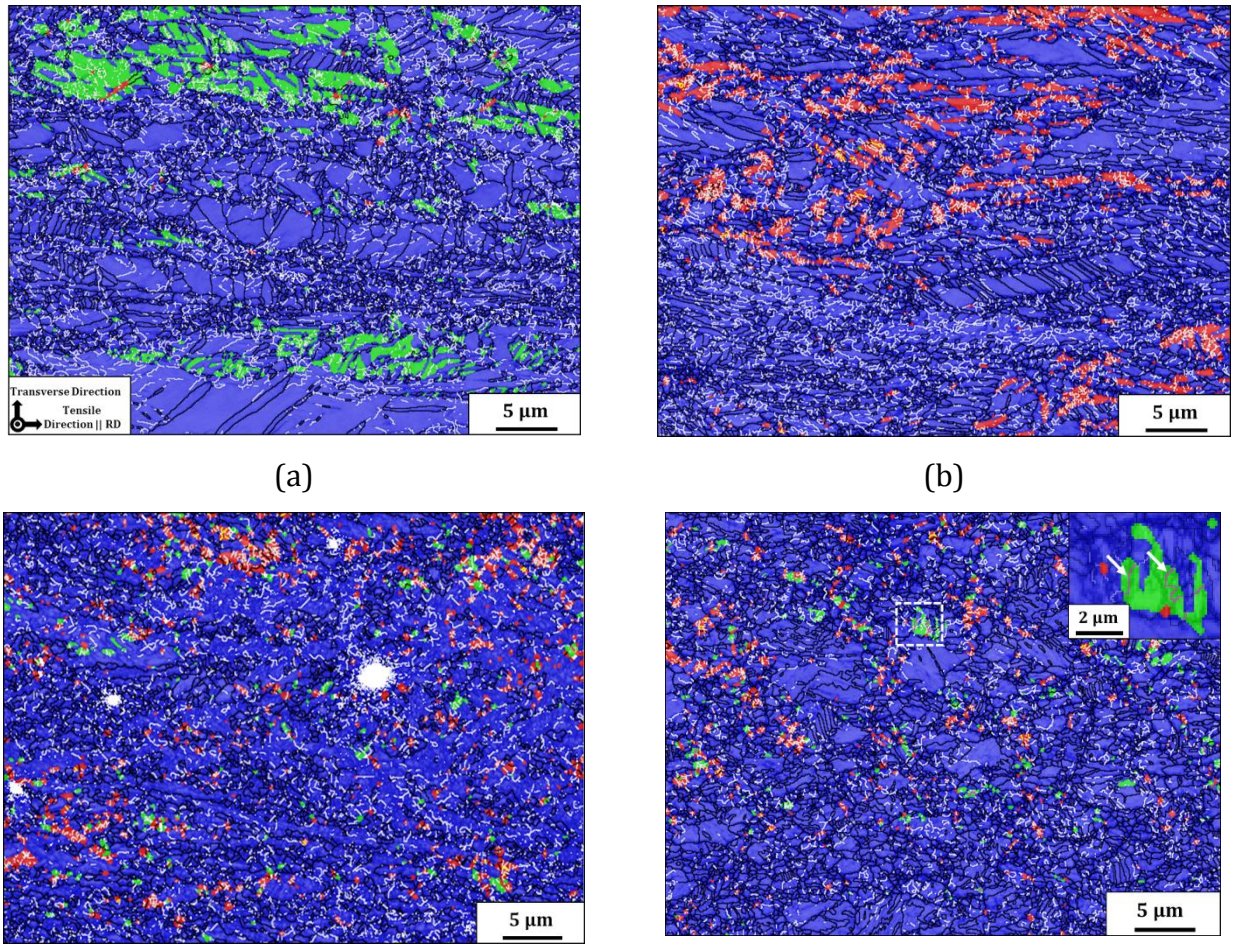

(a) (b)

(c) (d)

Figure 2: Superimposed band contrast and phase maps after subjecting to uniaxial tension of

the samples after (a) cold rolling and annealing at (b) 500 °C, (c) 625 °C and (d) 700 °C. Red = γ, green = ε-martensite, blue = α′-martensite, white = unindexed regions, silver = LAGBs, black = HAGBs and yellow = γ twin boundaries. Fig. 2d (inset) is from the white dashed square region showing $\{10\bar{1}2\}\langle\bar{1}011\rangle_{\varepsilon}$ extension twins in ε-martensite highlighted by white arrows in the inset.

The misorientation angle distributions before and after tensile testing of the γ, ε and α′-martensite phases, respectively, are shown in Figs. 3a-3c. All the phases recorded an increase in LAGBs fraction; signifying load partitioning between them upon uniaxial tension.

In the case of the 625 and 700 °C samples, γ bears the load during the early stages of tension and subsequently transformed to ε and α′-martensite. With higher tensile strain, deformation is accommodated by γ and its transformation as well as by the newly formed ε and α′-martensite.

In the case of the 500, 625 and 700 °C samples, the γ recorded a decline in the $60°/\langle 111\rangle_{\gamma}$ twin fraction upon uniaxial tension. In a similar vein, α′-martensite also showed a decline in the inter-variant boundary fraction after tension (for example, the peaks at $50°/\langle 110\rangle_{\alpha'}$, $60°/\langle 111\rangle_{\alpha'}$ and $60°/\langle 110\rangle_{\alpha'}$. For a comprehensive list, please refer to the Table 3 of Ref. [36]). Both the phenomena can be ascribed to the decays in the twin/matrix or inter-variant misorientation relationships because of the ever larger local lattice rotations needed to maintain strain compatibility when dislocations continuously accumulate at the annealing twin [37] or inter-variant boundaries during tension. On the other hand, ε-martensite recorded the appearance of a small peak between 86°-90° around the $\langle 11\bar{2}0\rangle_{\varepsilon}$ axis after tension; corresponding to $\{10\bar{1}2\}\langle\bar{1}011\rangle_{\varepsilon}$ extension twinning. $\{10\bar{1}2\}\langle\bar{1}011\rangle_{\varepsilon}$ extension twin formation in ε-martensite has also been observed during the plane strain compression of the present steel to 20% thickness reduction [34]. Parallel $\{10\bar{1}2\}\langle\bar{1}011\rangle_{\varepsilon}$ extension twins with similar orientations were observed inside a single ε-martensite lath during the uniaxial

tension of an Fe-15Mn-0.005C steel [28]. The formation of $\{10\bar{1}2\}\langle\bar{1}011\rangle_\varepsilon$ extension twins at the intersection of different ε-martensite variants were detected in an Fe-30Mn-6Si shape memory alloy [38]. In that study, four different $\{10\bar{1}2\}\langle\bar{1}011\rangle_\varepsilon$ extension twin variants of ε-martensite were observed.

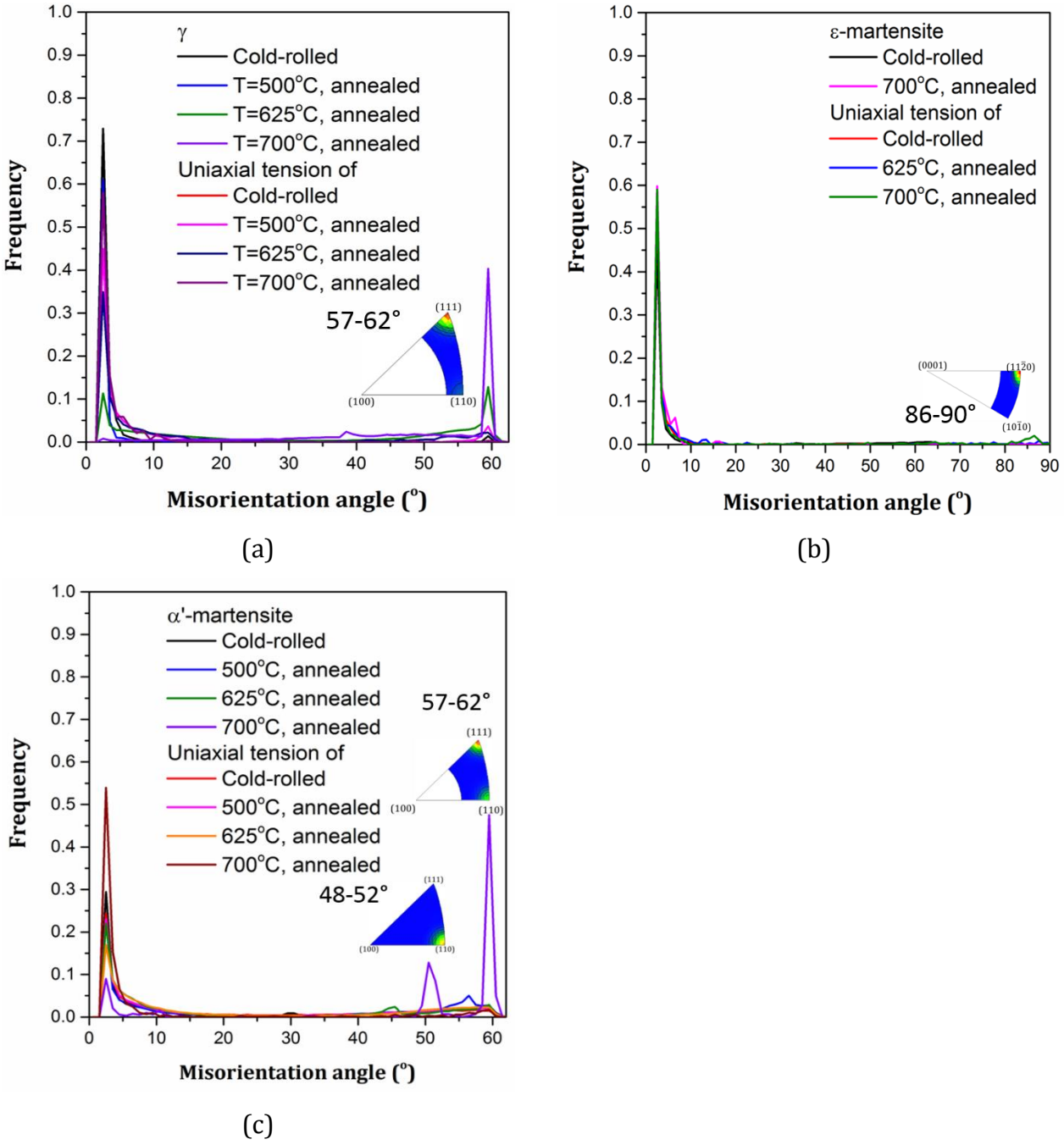

Figure 3: Misorientation angle distributions for (a) γ, (b) ε-martensite and (c) α′-martensite before and after tension for the cold-rolled and 500, 625 and 700 °C annealed samples.

3.2 Changes in micro-texture before and after tension

Fig. 4 denotes the experimental $\{111\}_{\gamma}$, $\{100\}_{\gamma}$, $\{0001\}_{\varepsilon}$ and $\{110\}_{\alpha'}$ pole figures of the cold-rolled and annealed conditions before (Figs. 4a, 4c, 4e and 4g) and after (Figs. 4b, 4d, 4f and 4h) tension; with the tensile axis parallel to the RD. With respect to ε and α′-martensite, the missing pole figures are ascribed to their small phase fractions returned for particular conditions. Consequently, the $\{0001\}_{\varepsilon}$ pole figures using the $[10\bar{1}0]_{\varepsilon}$ || RD and $[0002]_{\varepsilon}$ || ND plotting convention are shown only for the cold-rolled and 625 °C conditions after tension whereas the $\{110\}_{\alpha'}$ pole figure for the 700 °C condition before tension is not provided.

In the case of γ in the cold-rolled condition (Fig. 4a), the red dashed lines connect the A_{γ} ($\{110\}\langle 111\rangle_{\gamma}$) and Copper ($Cu_{\gamma}$, $\{112\}\langle 111\rangle_{\gamma}$) orientations of the $\langle 111\rangle_{\gamma}$ partial fibre while the blue dash-and-dot lines connect the Goss (G_{γ}, $\{110\}\langle 001\rangle_{\gamma}$) and Cube ($C_{\gamma}$, $\{001\}\langle 100\rangle_{\gamma}$) orientations of the $\langle 100\rangle_{\gamma}$ partial fibre; both of whom are parallel to the macroscopic tensile axis. Superimposing the ideal fcc orientations and partial fibres onto the $\{0001\}_{\varepsilon}$ and $\{110\}_{\alpha'}$ pole figures illustrated the prevalence of the Shoji-Nishiyama (S-N, [39]), Burgers [40] and Kurdjumov-Sachs (K-S, [41]) orientation relationships between the parent γ and daughter ε and α′-martensite phases (Fig. 4a) defined as $\{111\}_{\gamma}$ || $\{0001\}_{\varepsilon}$ || $\{110\}_{\alpha'}$ and $\langle 110\rangle_{\gamma}$ || $\langle 11\bar{2}0\rangle_{\varepsilon}$ || $\langle 111\rangle_{\alpha'}$.

The uniaxial tension of γ resulted in the typical development of a relatively stronger $\langle 111\rangle_{\gamma}$ and a weaker $\langle 100\rangle_{\gamma}$ double-fibre texture parallel to the tensile axis [42] comprising Brass (Br_{γ}, $\{110\}\langle 112\rangle_{\gamma}$), Cu_{γ} and G_{γ} orientations. Similar texture developments were reported for an Fe-18.4Mn-3.2Si-3Al steel subjected to uniaxial tension up to 0.4 true strain [43] and an Fe-17Mn-3Al-2Si steel [33] cycled between +0.035 and -0.028 true strains. The evolution of the relatively strong $\langle 111\rangle_{\gamma}$ and weak $\langle 100\rangle_{\gamma}$ fibres were ascribed to the increase in the latent hardening on non-coplanar systems, which in turn promotes co-planar slip and resulted in an overall weakening of the $\langle 100\rangle_{\gamma}$ fibre [44].

The phase transformation of the above γ orientations via the S-N orientation relationship resulted in the $\{01\bar{1}3\}\langle 1\bar{1}01\rangle_{\varepsilon}$ orientation shown in the $\{0001\}_{\varepsilon}$ pole figure (Fig. 4a). This orientation can also be denoted as $\{0001\}_{\varepsilon}$ poles deviated by ~24°-30° towards the RD (or tensile axis) belonging to the $\{hkil\}_{\varepsilon}$-fibre [45]. The retention of the $\{01\bar{1}3\}\langle 1\bar{1}01\rangle_{\varepsilon}$ orientation before and after tension highlights the metastable, deformation-induced nature of its formation.

On the other hand, the phase transformation of the above γ and ε-martensite orientations to α′-martensite orientations via the K-S and Burgers orientation relationships, respectively and the subsequent deformation accommodation by α′-martensite upon uniaxial tension results in the development of the $\langle 110\rangle_{\alpha'}$ || ND fibre. Along this fibre, the relatively stronger intensities around the $(001)[1\bar{1}0]_{\alpha'}$ and $(112)[1\bar{1}0]_{\alpha'}$ orientations can be attributed to their origin from: (i) the Br_{γ} and Cu_{γ}, G_{γ} orientations, respectively, or (ii) $\{hkil\}_{\varepsilon}$ -fibre orientations.

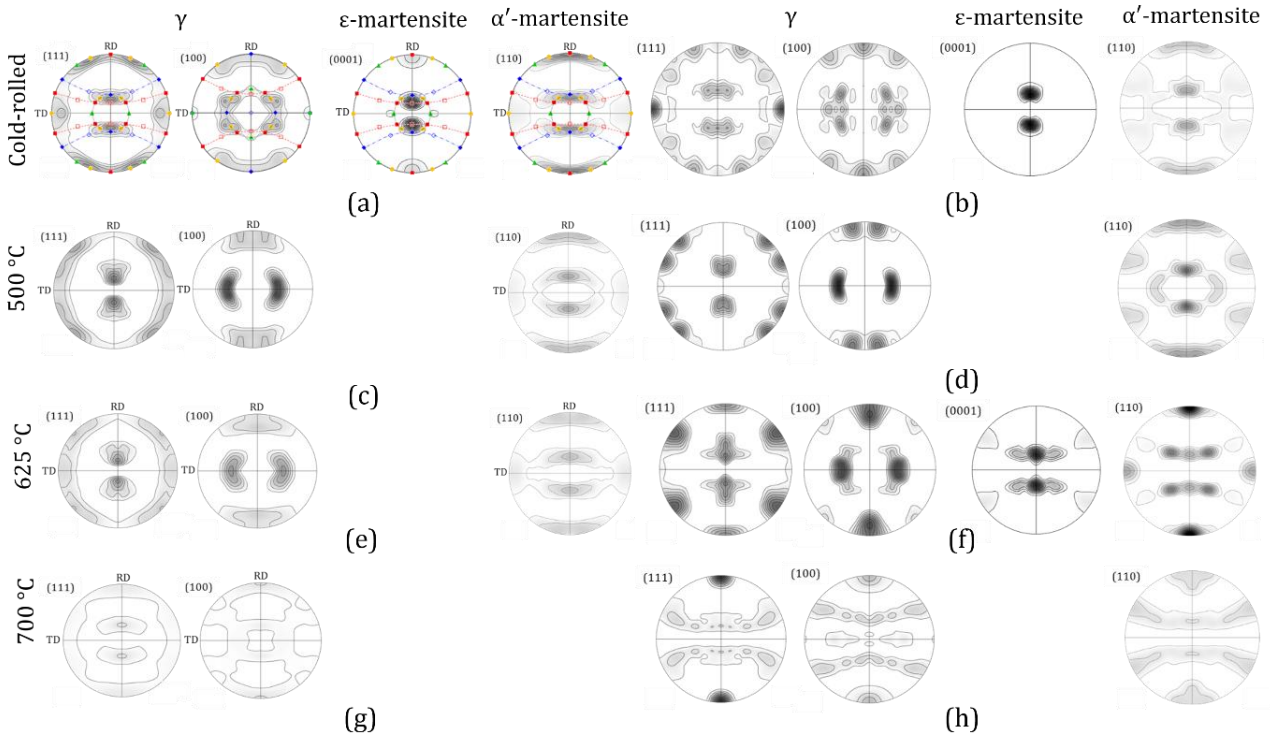

Figure 4: γ, ε and α′-martensite pole figures after (a, b) cold rolling and annealing at (c, d) 500 °C, (e, f) 625 °C and (g, h) 700 °C, (a, c, e, g) before and (b, d, f, h) after tension. In Fig. 4a, the ideal fcc orientations on the $\{111\}_\gamma$ pole figure are superimposed on the $\{0001\}_\varepsilon$ and $\{110\}_{\alpha'}$ pole figures. Also in Fig. 4a, the ideal fcc orientations are superimposed on the $\{100\}_\gamma$ pole figure. Key: ◆ $G_\gamma = \{110\}\langle001\rangle_\gamma$, ◇ $C_\gamma = \{001\}\langle100\rangle_\gamma$, □ $Cu_\gamma = \{112\}\langle111\rangle_\gamma$, ■ $A_\gamma = \{110\}\langle111\rangle_\gamma$, ● $Br_\gamma = \{110\}\langle112\rangle_\gamma$, ▲ $Rt\text{-}G_\gamma = \{011\}\langle011\rangle_\gamma$. In Figs. 4b, 4d, 4f, 4h, RD || tensile axis = vertical. Contours levels = 0.5×.

3.3 Mechanical properties after cold rolling and annealing

Figs. 5a and 5b are the true stress-strain and strain hardening curves, respectively, of the cold-rolled and annealed samples. The DIC-based Young's moduli of elasticity for the cold-rolled and 500, 625 and 700 °C samples are 201, 198, 196 and 194 GPa, respectively. The differences in elastic moduli are due to the variation in γ, ε and α′-martensite phase fractions for the different conditions. The elastic modulus of α′-martensite is greater than that of γ due to the coupling of the electron spin moments owing to the ferromagnetic nature of α′-martensite [46]. Thus during annealing, a decrease in the elastic modulus is observed due to the decrease of the α′-martensite fraction.

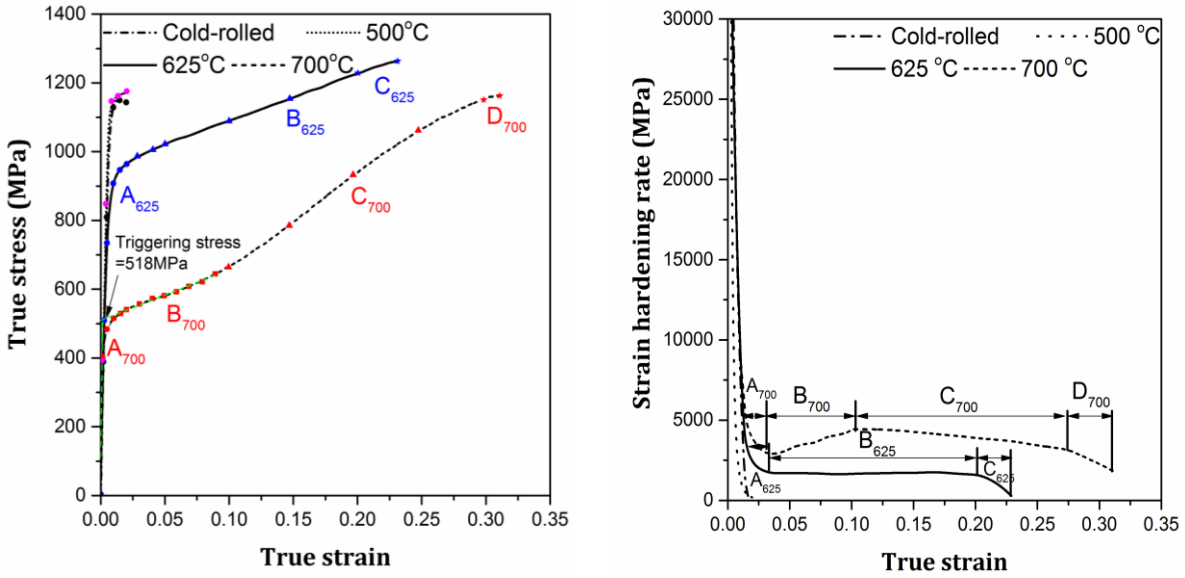

(a) (b)

Figure 5: (a) Macroscopic true stress-strain and (b) strain hardening curves for the cold-rolled and 500, 625 and 700 °C annealed samples.

It is apparent that the cold-rolled and 500 °C samples fail at ~0.02 true strain, almost immediately after reaching the high yield stresses (1080 ± 3 and 1075 ± 4 MPa, respectively, at 0.002 proof stress). This is attributed to the inability of the

predominantly α′-martensite microstructures to sustain further tension because of their cold-worked and incompletely recovered states, respectively.

On the other hand, the true stress-strain and strain hardening plots of the 625 and 700 °C samples are remarkably different. In the case of tension after 625 °C annealing, the initial approximately dual-phase, metastable γ + α′-martensite microstructure (Fig. 1c) undergoes yielding at 810 ± 5 MPa followed by an approximately linear increase in the stress values up to a UTS of 1237 ± 3 MPa at 0.23 true strain. The corresponding strain hardening curve in Fig. 5b can be roughly divided into Regions A_{625} (blue circles), B_{625} (blue triangles) and C_{625} (blue stars) comprising: (i) the elasto-plastic transition, (ii) an approximate flat-lining in the strain hardening curve followed by, (iii) a reduction in the strain hardening rate with increasing true strain, respectively.

Comparable true stress-strain and strain hardening curves were obtained in other Mn steel with an initial dual-phase microstructure [47]. In that study upon tension, the formation of ε and α′-martensite at γ grain boundaries took place followed by the transformation of adjacent γ and ε-martensite to α′-martensite.

Upon uniaxial tension after 700 °C annealing, resulted in the almost single-phase metastable γ microstructure (Fig. 1d), yielding at ~465 ± 4 MPa, followed by a slow rise in the true stress values up to a UTS of ~1121 ± 3 MPa at 0.31 true strain. The slow rise in the true stress is associated with the initiation and progress to deformation-induced ε and α′-martensite formation. The intersection of the linearly extrapolated elastic modulus and the tangent drawn to the slow rising stress region is defined as the triggering stress for this phenomenon [48] and was found to be ~518 MPa. The corresponding strain hardening curve in Fig. 5b can be roughly divided into Regions A_{700} (red circles), B_{700} (red squares), C_{700} (red triangles) and D_{700} (red stars) comprising: (i) the elasto-plastic transition, (ii) pronounced strain hardening, (iii and iv)

varying rates of reduction in strain hardening with increasing true strain, respectively. Similarly shaped stress-strain curves were obtained upon the tension of other metastable austenitic stainless steels [13, 49-52].

The Region A corresponds to the reduction in strain hardening rate due to elasto-plastic transition is accompanied by the initiation of partial slip in γ via the motion of Shockley partial dislocations. It follows that for the 625 and 700 °C conditions, Region B corresponds to the phase transformation of metastable γ to ε and α′-martensite and strain hardening caused by the concurrent reductions in the mean free path for dislocation glide in the three phases. In-situ neutron diffraction during the monotonic uniaxial tensile loading of the present steel after cold rolling and subsequent annealing at 900 °C also displayed the decrease in the fraction of γ with an increase in the fraction of ε and α′-martensite at true strains greater than ∼0.025 and ∼0.05, respectively, as shown in Fig. 2c of Ref. [33]. Alternatively, the Regions C_{625}, C_{700} and D_{700} correspond to lower rates of phase transformation and the inability of the deformation-induced ε and α′-martensite phases to sustain/accommodate further tension.

The distinct difference in the strain hardening Region B_{625} compared to the Region B_{700} was due to the additional strain hardening capacity from the pre-existing α′-martensite [47] accompanied by the transformation of γ to ε and α′-martensite in the Region B_{625}. However, the pronounced strain hardening in Region B_{700} was only due to the phase transformation of γ.

3.4 DIC of the cold-rolled and annealed samples during tension

The distribution of axial true strains along the entire gauge length and up to the UTS of the cold-rolled and 500, 625 and 700 °C samples are presented in Figs. 6, 7a, 7b, 8a-8c. The distribution of shear strains up to the UTS for the 625 and 700 °C samples are

displayed in Figs. 7c, 8d. The transverse true strains were omitted as they mirror their axial true strain counterparts.

In the cold-rolled and 500 °C samples (Fig. 6), the axial true strain distribution was approximately uniform up to 0.005 macroscopic true strain followed by the onsets of localised plastic deformation and strain localisation at ~0.01 and ~0.015 macroscopic true strains, respectively. The strain localisation due to the onset of necking, manifested as higher axial true strains compared to the average macroscopic true strain value across the gauge length. For example, in Figs. 6a, 6b, at 0.02 macroscopic true strain, the maximum true strain in the strain localised region was ~0.03. The early necking at 0.02 macroscopic true strain was also observed from the DIC axial true strain distributions in Figs. 6a and 6b for both the cold-rolled and 500 °C samples. This can be attributed to microstructures of the samples in Figs. 2a and 2b containing predominantly α′-martensite in the cold-rolled and incompletely recovered states for the cold-rolled and 500 °C samples, respectively.

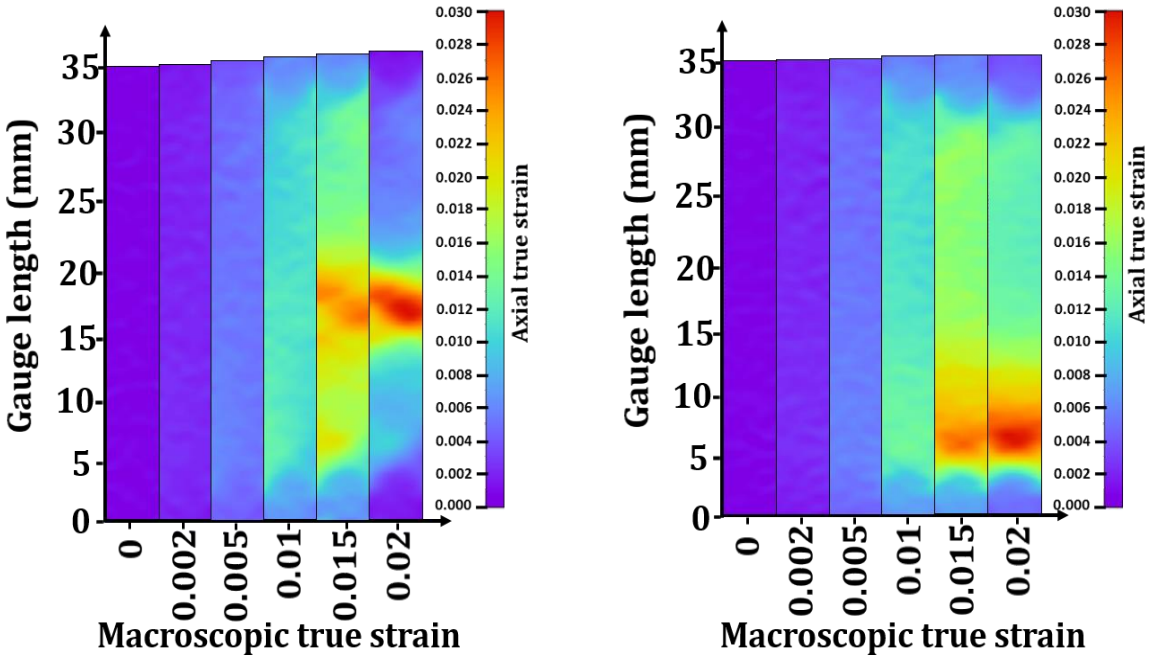

(a) (b)

Figure 6: Digital image correlation axial true strain distribution maps of the (a) cold-rolled and (b) 500 °C annealed sample.

In the case of the 625 and 700 °C samples (Figs. 7a, 7b, 8a and 8b), ~0.015 and ~0.01 macroscopic true strains, respectively, correspond to the end of the Regions A_{625} and A_{700}, at which point the distribution in axial strains remains approximately uniform. Since these macroscopic true strains are higher than the strain at yield, here nominally defined as the 0.002 axial true strain, the above results were in contrast to Eskandari et al. [12]. That study reported a strain localisation before macroscopic yielding in a TRIP-TWIP steel subjected to uniaxial tension and ascribed it to the γ to ε-martensite transformation.

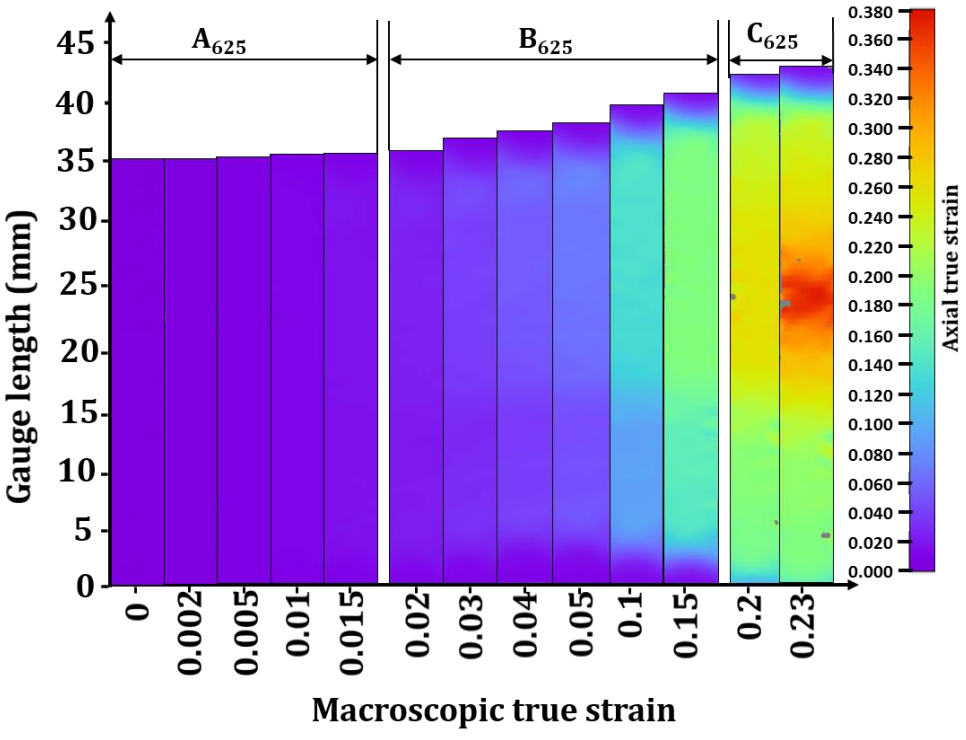

(a)

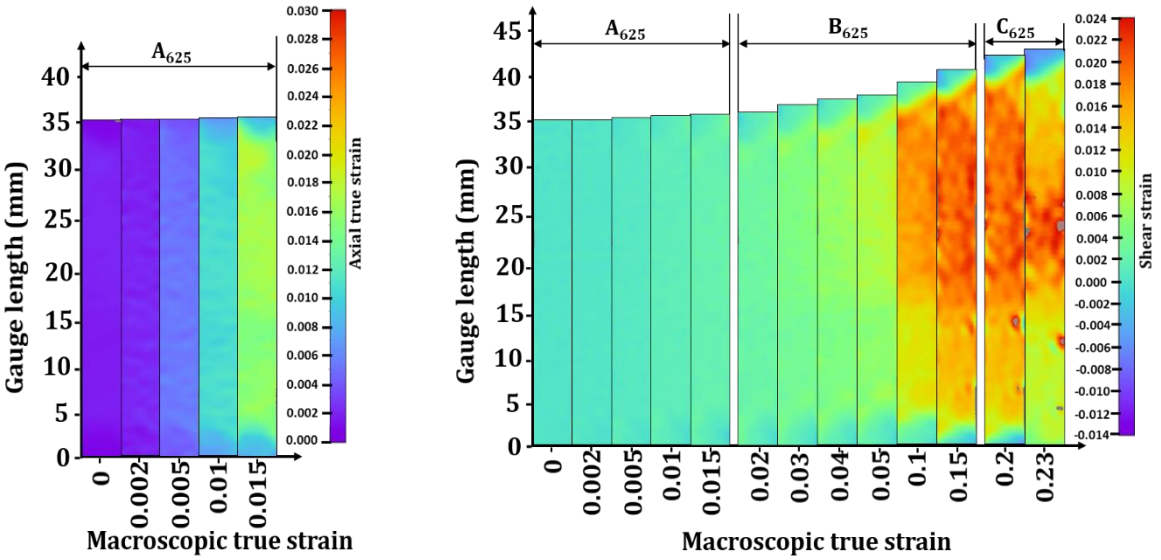

(b) (c)

Figure 7: Digital image correlation maps for the 625 °C annealed sample presenting the distribution of (a, b) axial true strain and (c) shear strain. Fig. 7b is the scaled axial true strain distribution of the Region A_{625} in Fig. 7a.

It follows that in the present steel, the phase transformation of metastable γ to ε and α′-martensite and the variation in load partitioning between the three phases coincided with localisations in the axial and shear strain values beyond ~0.01-0.015 macroscopic true strain (or the beginning of Regions B_{625} and B_{700}). μ-DIC axial strain mapping showed a higher strain in γ compared to α′-martensite indicating strain partitioning in an Fe-12Mn-3Al-0.05C steel upon uniaxial tension [53]. This was attributed to the transformation of γ to ε and α′-martensite and a lower rate of dynamic recovery in γ. Dutta et al. [53] also reported that during uniaxial tension to 0.05 and 0.07 strains, γ accommodated the majority of the strain. However, after uniaxial tension to strains greater than 0.07, the α′-martensite accommodated higher strains compared to γ.

The end of Regions B_{625} and C_{700} corresponds to true strains by which a large fraction of γ transformed to deformation-induced α′-martensite. However, the transformation continued into Regions C_{625} and D_{700} at a slower rate. From the microstructures which

correspond to the end of Regions C_{625} and D_{700} shown in Figs. 2c and 2d respectively, it can be observed that the majority of γ transformed to deformation-induced α′-martensite. The α′-martensite accommodated tensile deformation via a localised increase in axial and shear strains (Fig. 8d); which in turn manifested as a wide plastic band of high axial true strain values upon reaching the UTS.

Fig. 8e highlights the effect of tensile sample geometry on phase transforming steels using the 700 °C sample as an example. For different macroscopic true strains, the axial true strains recorded in the middle of the sample cross-section (along line A-A′ in Fig. 8a) was plotted across the gauge length. It was apparent that up to ~0.1 macroscopic true strain, the axial true strains was on average, higher nearer the grips (between ~0-9 mm and ~27-35 mm, light grey and light orange regions) than the middle of the gauge length (between ~9-27 mm, light green region Fig. 8e). Here at 0 and 35 mm, the axial true strains recorded their lowest values, followed by a local maxima at ~3 and ~33 mm (light grey regions, Fig. 8e) and thereafter, decreased up to ~9 and ~27 mm (light orange regions, Fig. 8e) to values that span the middle of the gauge length across ~9-27 mm (light green region, Fig. 8e).

Between ~0.15-0.25 macroscopic true strains, the lowest axial true strains were again closest to the grips at 0 and 35 mm which increased up to ~3 and ~33 mm (light blue regions, Fig. 8e) to approximately uniform values between ~3-33 mm of the gauge length (light aqua region, Fig. 8e).

Beyond ~0.3 macroscopic true strain, the lowest axial true strains are closest to the grips at 0 and 35 mm which increased up to ~3 and ~30 mm. However, at these macroscopic true strains, the axial true strains are non-uniform between ~3-30 mm of the gauge length.

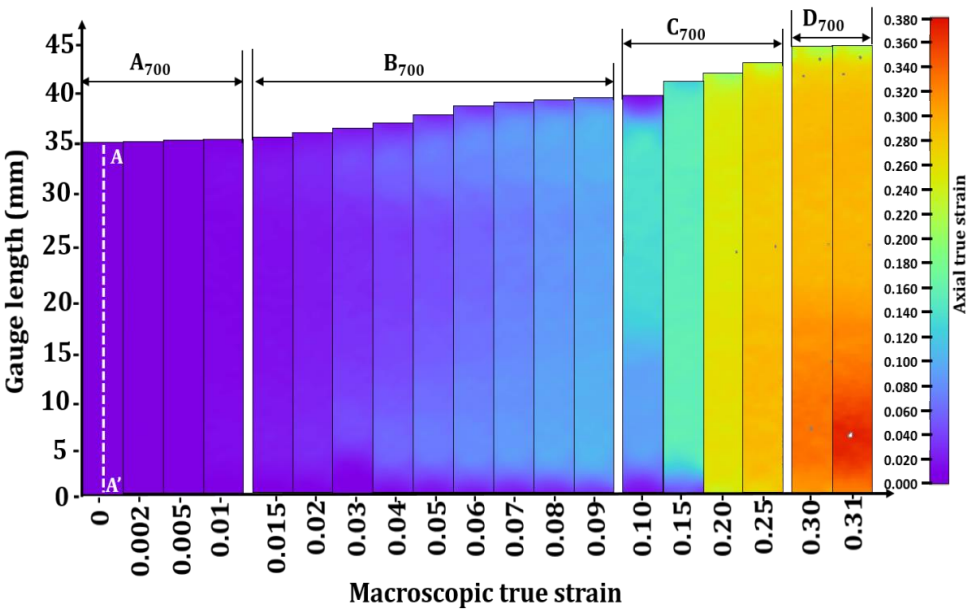
A700
B700
C700
D700
A
A'
Gauge length (mm)
Macroscopic true strain
Axial true strain

(a)

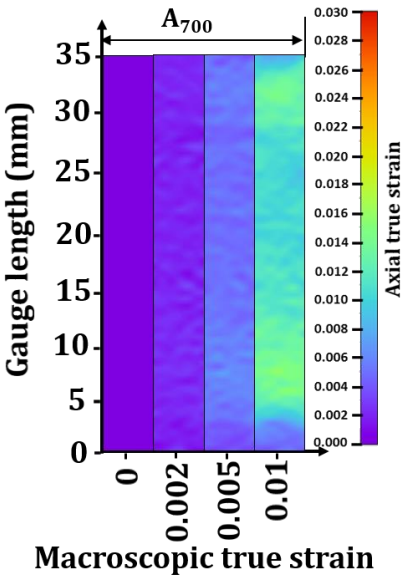
A700
Gauge length (mm)
Macroscopic true strain
Axial true strain

(b)

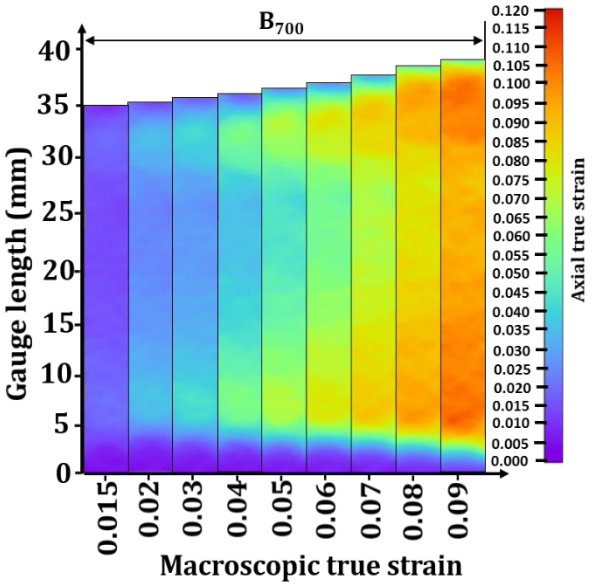
B700
Gauge length (mm)
Macroscopic true strain
Axial true strain

(c)

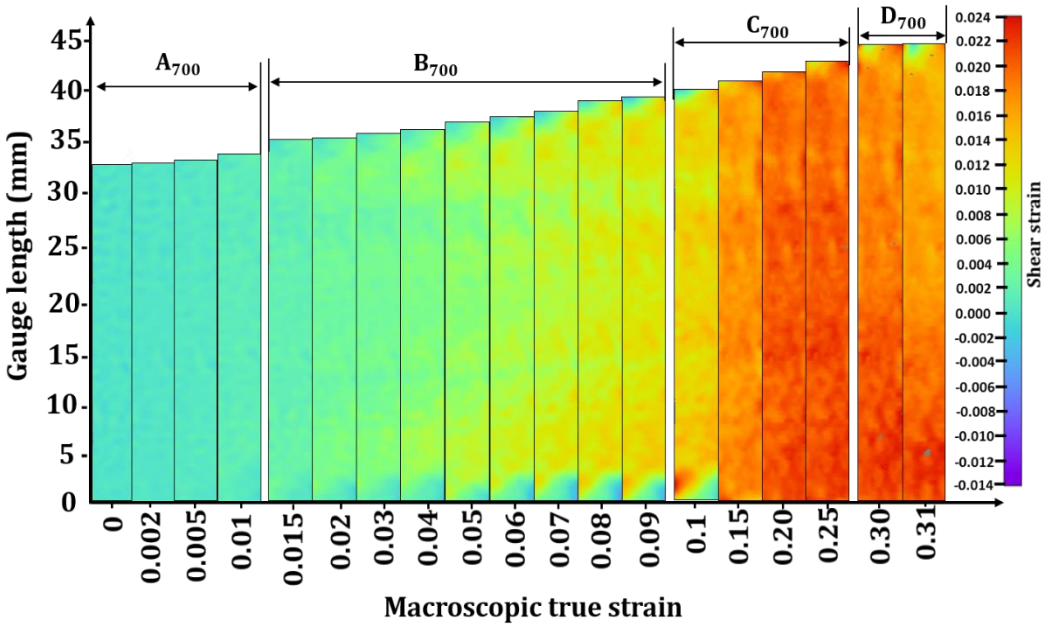

(d)

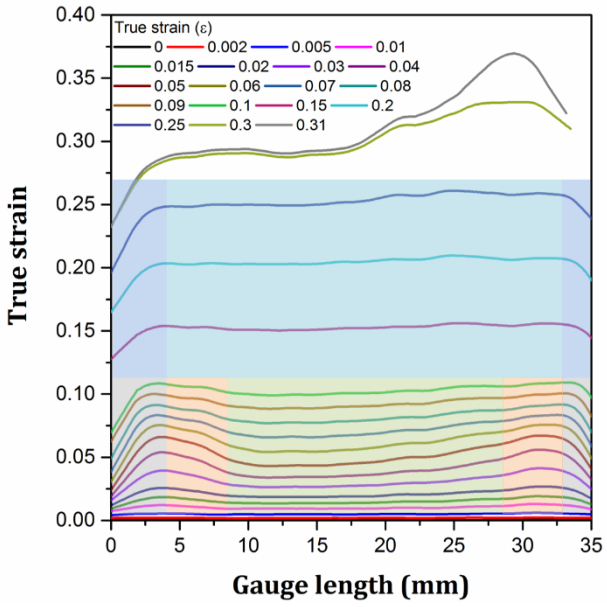

(e)

Figure 8: Digital image correlation maps for the 700 °C annealed sample presenting the distribution of (a, b, c) axial true strain, (d) shear strain and (e) axial true strain along the line A-A′ in Fig. 8a. Figs. 8b and 8c are the scaled axial true strain distribution of the Regions A_{700} and B_{700}, respectively, of Fig. 8a. The Regions light grey, light blue show increasing, light orange show decreasing, light green, aqua show uniform axial true strain distribution along the gauge length in Fig. 8e.

A similar strain localisation along the gauge length was also observed upon the tension of an Fe-21Mn-2.5Si-1.6Al-0.11C steel [12] and was ascribed to the localised transformation of γ to deformation-induced α′-martensite. The latter was verified by magnetic measurements along the gauge length. The fraction of γ decreased at the ends of the gauge length closest to the grips due to the early onset of phase transformation brought on by the stress concentration effects associated with the geometry of the dog-bone shaped tensile sample. Similarly, the stress concentration at the ends of the gauge length was linked with strain localisation by the transformation of γ to α′-martensite [8].

It was reported [8] that DIC axial strain localisation in the stress plateau region of the stress-strain curve in an Fe-7Mn-0.14C-0.23Si steel was observed during the transmission of Lüders bands. In that steel, within the Lüders bands, the transformation of γ to deformation-induced α′-martensite also took place simultaneously [8]; for which the γ volume fraction decreased from 29% to 9% which was confirmed by XRD. Thermal measurements via infrared thermography also showed a higher heat dissipation during the propagation of Lüders bands which was ascribed to martensite transformation. In addition, the microstructure within the Lüders bands showed the transformation of γ to α′-martensite compared to the microstructure outside the Lüders bands. Furthermore, the regions deformed by the propagation of Lüders bands demonstrated an increase in hardness due to the transformation of γ to α′-martensite. In that study, PLC bands were also observed but were associated with serrations in the strain hardening region occurring after the stress plateau region of the tensile stress-strain curve.

A similar transformation of γ to α′-martensite was recorded by XRD during the interrupted tensile testing of an Fe-7Mn-2Al-0.3C steel annealed at 720 °C for 3600 s

which resulted in strain localisation by the propagation of PLC bands [54]. However, the formation of α′-martensite also led to the strong resistance to the transmission of PLC bands. Thus, the PLC bands were observed to propagate discontinuously across the gauge section [54].

Lüders band propagation was also witnessed in an Fe-7Mn-0.14C-0.23Si steel during uniaxial tension at room temperature and also at 100 and 300 °C [55]. Martensite transformation took place during tensile testing at room temperature however, it did not proceed when uniaxial tension was performed at 100 and 300 °C. Thus, strain localisation could be also caused only by the propagation of Lüders band without the occurrence of martensite transformation [55]. However, in the present investigation, strain localisation was attributed only to martensite transformation as shown in Figs. 2c and 2d without the propagation of Lüders or PLC bands.

DIC axial strain localisation was also observed during the uniaxial tension of an Fe-21Mn-2.5Si-1.6Al-0.11C-0.02Nb-0.02Ti-0.01V steel deformed to 0.02 and 0.025 true strains at strain rates of 0.001 and 0.003 s^{-1}, respectively [11]. Optical and EBSD micrographs of the microstructure at strain rates of 0.001 and 0.003 s^{-1} at 0.02 and 0.025 true strains showed the formation of only ε-martensite without the formation of α′-martensite. Thus, the transformation of γ to ε-martensite could also lead to strain localisation.

In-situ neutron diffraction accompanied tensile testing of the present steel sample annealed at 900 °C showed the formation of α′-martensite at a macroscopic strain of 0.05 which is at the middle of the slowly rising stress region [33]. The onset of γ to ε-martensite transformation was also recorded at ~0.025 macroscopic strain before the start of ε to α′-martensite transformation [33]. Thus, the strain localisation can be ascribed to the onset of both γ to ε-martensite and ε to α′-martensite transformations.

Once the γ is activated for phase transformation, it manifested as regions of high-strain concentration (in red, Fig. 8e) propagating along the gauge length from 3 and 33 mm positions towards the centre of the gauge section between 0.02-0.1 macroscopic true strains; resulting in the slow rising stress Region B_{700} seen in Fig. 5a. The local axial true strains immediately in front of the propagating local maxima were lower than the macroscopic true strain in Fig. 8e. This was ascribed to a local partitioning effect; whereby the greater strain accommodated by the γ transforming into ε and α′-martensite within the local maxima region resulted in the lower axial strains in their immediate vicinity. Consequently, the local maxima regions propagated towards the middle of the gauge length until the macroscopic true strain becomes approximately equal throughout its span in Fig. 8e.

3.5 Fractography

Figs. 9a, 9c, 9e are the representative secondary electron images of the fracture surfaces of the cold-rolled and 625 and 700 °C sample cross-sections after uniaxial tension, respectively, with the zoomed-in views displayed in Figs. 9b, 9d, 9f. In the cold-rolled sample, secondary cracks (see red arrow in Fig. 9a) along with flat ledge-like morphologies in local areas of the fracture cross-section (see red arrow in Fig. 9b) can be observed on the fracture surface of the cold-rolled sample. It depicts quasi-cleavage formed by rapid crack propagation in α′-martensite [56] and shallow dimples; reminiscent of mixed brittle and ductile fracture modes. The fracture surface of the 500 °C was similar to the cold-rolled sample and therefore not shown.

Alternatively, the 625 °C (Figs. 9c, 9d) and 700 °C (Figs. 9e, 9f) samples records ledge-like morphologies and rugged facets. The magnified views (Figs. 9d, 9f) of these conditions show shallow dimples indicative of ductile fracture [57-59] and voids caused

by particle pull out (see red arrow in Fig. 9d). In Fig. 9f, coarse particles of ~5 μm size are present in the voids. On coalescence, micro-voids (see red arrow in Fig. 9f) can lead to the formation of shallow dimples.

Characterisation of the fracture surfaces of an Fe-22Mn-0.6C-0.2V steel also showed the presence of submicron sized dimples indicating limited void growth [60]. The voids nucleated around fine spherical precipitates of vanadium carbide or at the intersection points between vanadium carbide precipitate and fine twins. Investigation of the fracture surfaces on an Fe-22.3Mn-0.6C-0.2Si high Mn steel demonstrated the propagation of quasi-cleavage cracks or formation of a sheet of voids. The voids were less than 1 μm size and were free from inclusions [61].

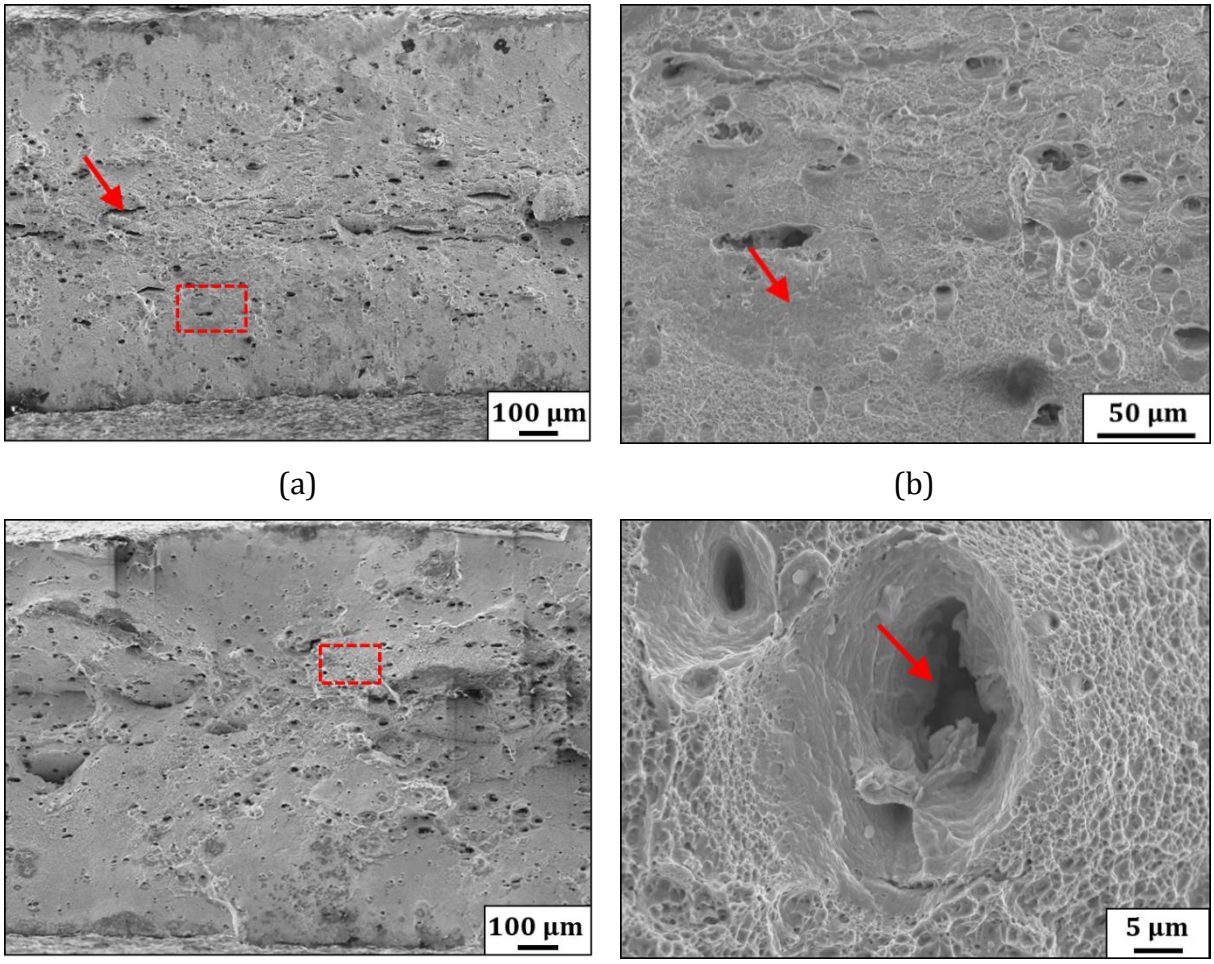

(a) (b)

(c) (d)

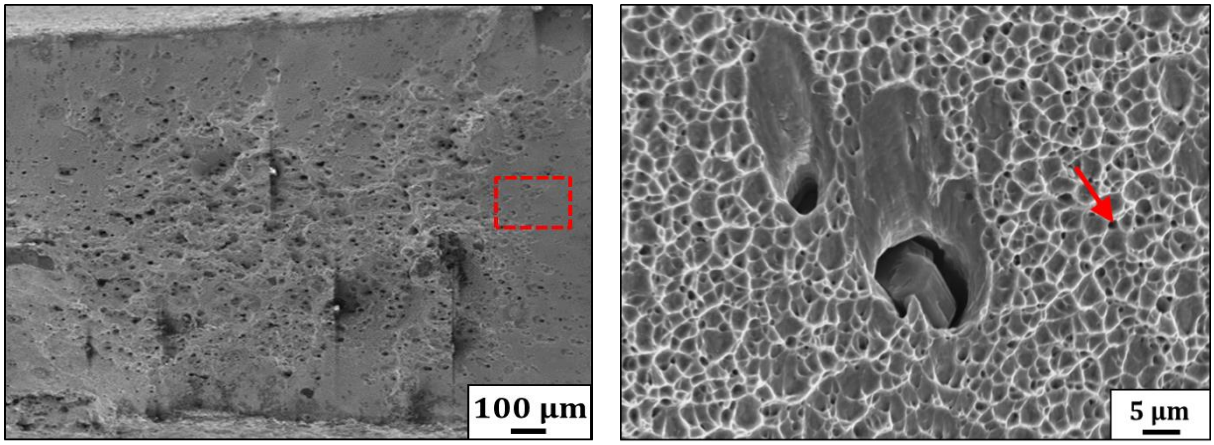

(e) (f)

Figure 9: Fractography of the fractured tensile samples after (a, b) cold rolling, annealing at (c, d) 625 °C and (e, f) 700 °C. Figs. 9b, 9d, 9f are zoomed-in views of the regions highlighted by red dashed rectangles from Figs. 9a, 9c, 9e, respectively. The red arrows in Figs. 9a, 9b, 9d and 9f indicate secondary cracks, ledge-like morphologies, particle pull out and microvoids, respectively.

4. Conclusions

In the present investigation, characterisation via digital image correlation and electron back-scattering diffraction was undertaken on the tensile deformed samples of an Fe-17Mn-3Al-2Si-1Ni-0.06C steel after cold rolling to 42% thickness reduction and annealing at 500, 625 and 700 °C.

(1) The microstructures of the cold-rolled and 500 °C annealed samples containing predominantly α′-martensite in the cold-rolled and incompletely recovered states, respectively and either remnant ε-martensite or γ, remained unchanged upon uniaxial tension. For these two conditions, the axial true strain distribution was uniform followed by strain localisation at necking.

(2) Upon uniaxial tension, the transformation of initially reverted/recrystallised γ and recrystallised γ into ε and α′-martensite was observed in the 625 and 700 °C

annealed samples, respectively. The formation of $\{10\bar{1}2\}\langle\bar{1}011\rangle_{\varepsilon}$ extension twins in ε-martensite were also detected after uniaxial tension in the 700 °C annealed sample, which suggested the deformation of ε-martensite. During uniaxial tension, the axial true strain remained approximately uniform followed by strain localisation due to the phase transformation of metastable γ to ε and α′-martensite and the load partitioning among the three phases.

(3) The formation of $\langle 111\rangle_{\gamma}$, $\langle 100\rangle_{\gamma}$ double-fibre texture was observed in γ whereas ε and α′-martensite showed $\{hkil\}_{\varepsilon}$-fibre and $\langle 110\rangle_{\alpha'}$|| ND fibre, respectively, upon uniaxial tension.

(4) The fracture surfaces showed a mixed brittle and ductile fracture mode for the cold-rolled and 500 °C annealed samples, whereas 625 and 700 °C annealed samples exhibited ductile fracture mode.

Acknowledgements

This research was partially supported by the Australian Research Council (ARC, DP130101882). The authors are grateful to Dr. B. J. Davis, UOW for his help with the DIC experiments. The authors acknowledge the use of the JEOL JSM-7001F FEG-SEM located at the UOW Electron Microscopy Centre purchased with the financial support from the ARC (LE0882613).

Data availability: The raw/processed data cannot be shared at this time as the data also forms part of an ongoing study. However, some data could be provided on request.

Conflict of Interest: none

References

[1] C. Horvath, C. M. Enloe, J. Coryell, J. P. Singh, *New developments in advanced high strength sheet steel* **2017**, Colorado, US.

[2] F. Berrenberg, C. Haase, L. A. Barrales-Mora, D. A. Molodov, *Mater. Sci. Eng. A* **2017**, *681*, 56-64.

[3] K. Renard, S. Ryelandt, P. J. Jacques, *Mater. Sci. Eng. A* **2010**, *527*, 2969-2977.

[4] H. Y. Yu, S. M. Lee, J. H. Nam, S. J. Lee, D. Fabrègue, M. h. Park, N. Tsuji, Y. K. Lee, *Acta Mater.* **2017**, *131*, 435-444.

[5] J. Min, L. G. Hector Jr, L. Zhang, L. Sun, J. E. Carsley, J. Lin, *Mater. Design* **2016**, *95*, 370-386.

[6] X. Bian, F. Yuan, X. Wu, *Mater. Sci. Eng. A* **2017**, *696*, 220-227.

[7] M. Kang, J. Park, S. S. Sohn, H. S. Kim, N. J. Kim, S. Lee, *Mater. Sci. Eng. A* **2017**, *693*, 170-177.

[8] X. G. Wang, L. Wang, M. X. Huang, *Acta Mater.* **2017**, *124*, 17-29.

[9] X. G. Wang, L. Wang, M. X. Huang, *Mater. Sci. Eng. A* **2016**, *674*, 59-63.

[10] W. Wu, Y. W. Wang, P. Makrygiannis, F. Zhu, G. A. Thomas, L. G. Hector, X. Hu, X. Sun, Y. Ren, *Mater. Sci. Eng. A* **2018**, *711*, 611-623.

[11] M. Eskandari, M. R. Yadegari-Dehnavi, A. Z. Hanzaki, M. A. Mohtadi-Bonab, R. Basu, J. A. Szpunar, *Opt. Laser. Eng.* **2015**, *67*, 1-16.

[12] M. Eskandari, A. Z. Hanzaki, M. Yadegari, N. Soltani, A. Asghari, *Opt. Laser. Eng.* **2014**, *54*, 79-87.

[13] D. P. Escobar, S. S. F. Dafé, D. B. Santos, *J. Mater. Res. Tech.* **2015**, *4*, 162-170.

[14] Y. B. Das, A. N. Forsey, T. H. Simm, K. M. Perkins, M. E. Fitzpatrick, S. Gungor, R. J. Moat, *Mater. Design* **2016**, *112*, 107-116.

[15] B. Sun, N. Vanderesse, F. Fazeli, C. Scott, J. Chen, P. Bocher, M. Jahazi, S. Yue, *Scripta Mater.* **2017**, *133*, 9-13.

[16] M. Callahan, O. Hubert, F. Hild, A. Perlade, J. H. Schmitt, *Mater. Sci. Eng. A* **2017**, *704*, 391-400.

[17] C. C. Tasan, M. Diehl, D. Yan, C. Zambaldi, P. Shanthraj, F. Roters, D. Raabe, *Acta Mater.* **2014**, *81*, 386-400.

[18] C. C. Tasan, J. P. M. Hoefnagels, M. Diehl, D. Yan, F. Roters, D. Raabe, *Int. J. Plasticity* **2014**, *63*, 198-210.

[19] D. Yan, C. C. Tasan, D. Raabe, *Acta Mater.* **2015**, *96*, 399-409.

[20] P. J. Jacques, Q. Furnémont, F. Lani, T. Pardoen, F. Delannay, *Acta Mater.* **2007**, *55*, 3681-3693.

[21] L. M. Roncery, S. Weber, W. Theisen, *Steel Res. Int.* **2012**, *83*, 307-314.

[22] P. D. Zavattieri, V. Savic, L. G. Hector, J. R. Fekete, W. Tong, Y. Xuan, *Int. J. Plasticity* **2009**, *25*, 2298-2330.

[23] M. Kuntz, **2008,** Verformungsmechanismen hoch manganlegierter austenitischer TWIP-Stähle, Thesis Stuttgart University.

[24] A. Bäumer, **2009,** Verfestigungsverhalten von hochmanganhaltigen Stählen mit TWIP-Effekt / von Annette Bäumer, PhD Thesis, RWTH Aachen University.

[25] S. Wesselmecking, L. Tataurova, W. Bleck, *Advanced High-strength Steels, TMS Annual Meeting & Exhibition*, **2018**.

[26] S. Pramanik, A. A. Saleh, E. V. Pereloma, A. A. Gazder, *Mater. Charact.* **2018**, *144*, 66-76.

[27] G. Palumbo, K. T. Aust, *Acta Metall. Mater.* **1990**, *38*, 2343-2352.

[28] J. Chen, W. N. Zhang, Z. Y. Liu, G. D. Wang, *Mater. Sci. Eng. A* **2017**, *698*, 198-205.

[29] J. J. Fundenberger, B. Beausir, *JTEX software for texture analysis, University de Lorriane, Metz* **2015**.

[30] S. Pramanik, A. A. Saleh, D. B. Santos, E. V. Pereloma, A. A. Gazder, *IOP C. Ser.* **2015**, *89*, 012042.

[31] A. A. Gazder, A. A. Saleh, M. J. B. Nancarrow, D. R. G. Mitchell, E. V. Pereloma, *Steel Res. Int.* **2015**, *86*, 1204-1214.

[32] A. A. Gazder, A. A. Saleh, A. G. Kostryzhev, E. V. Pereloma, *Mater. Today: Proc.* **2015**, *2*, S647-S650.

[33] A. A. Saleh, D. W. Brown, E. V. Pereloma, B. Clausen, C. H. J. Davies, C. N. Tomé, A. A. Gazder, *Appl. Phys. Lett.* **2015**, *106*, 171911.

[34] S. Pramanik, A. A. Gazder, A. A. Saleh, E. V. Pereloma, *Mater. Sci. Eng. A* **2018**, *731*, 506-519.

[35] R. L. Bell, R. W. Cahn, *Proc. R. Soc. Lond. A* **1957**, *239*, 494-521.

[36] E. V. Pereloma, F. Al-Harbi, A. A. Gazder, *J. Alloy Compd.* **2014**, *615*, 96-110.

[37] S. K. Mishra, S. M. Tiwari, A. M. Kumar, L. G. Hector, *Metall. Trans. A* **2012**, *43*, 1598-1609.

[38] X. Zhang, T. Sawaguchi, *Acta Mater.* **2018**, *143*, 237-247.

[39] Z. Nishiyama, Elsevier Science, ***2012***.

[40] W. G. Burgers, *Physica* **1934**, *1*, 561-568.

[41] G. Kurdjumow, G. Sachs, *Z. Phys.* **1930**, *64*, 325-343.

[42] A. A. Saleh, E. V. Pereloma, B. Clausen, D. W. Brown, C. N. Tomé, A. A. Gazder, *Mater. Sci. Eng. A* **2014**, *589*, 66-75.

[43] P. Yang, T. Y. Liu, F. Y. Lu, L. Meng, *Steel Res. Int.* **2012**, *83*, 368-373.

[44] A. T. English, G. Y. Chin, *Acta Metal. Mater.* **1965**, *13*, 1013-1016.

[45] Y. N. Wang, J. C. Huang, *Mater. Chem. Phys.* **2003**, *81*, 11-26.

[46] S. Münstermann, Y. Feng, W. Bleck, *Can. Metall. Quart.* **2014**, *53*, 264-273.

[47] H. W. Yen, S. W. Ooi, M. Eizadjou, A. Breen, C. Y. Huang, H. K. D. H. Bhadeshia, S. P. Ringer, *Acta Mater.* **2015**, *82*, 100-114.

[48] T. W. Duerig, J. Albrecht, D. Richter, P. Fischer, *Acta Metal. Mater.* **1982**, *30*, 2161-2172.

[49] H. Ding, H. Ding, D. Song, Z. Tang, P. Yang, *Mater. Sci. Eng. A* **2011**, *528*, 868-873.

[50] M. C. McGrath, D. C. Van Aken, N. Medvedeva, J. E. Medvedeva, *Metall. Trans. A* **2013**, *44*, 4634-4643.

[51] A. Arlazarov, M. Gouné, O. Bouaziz, A. Hazotte, G. Petitgand, P. Barges, *Mater. Sci. Eng. A* **2012**, *542*, 31-39.

[52] P. Behjati, A. Kermanpur, L. P. Karjalainen, A. Järvenpää, M. Jaskari, H. S. Baghbadorani, A. Najafizadeh, A. Hamada, *Mater. Sci. Eng. A* **2016**, *650*, 119-128.

[53] A. Dutta, D. Ponge, S. Sandlöbes, D. Raabe, *Advanced High-strength Steels, TMS Annual Meeting & Exhibition*, **2018.**

[54] F. Yang, H. Luo, E. Pu, S. Zhang, H. Dong, *Int. J. Plasticity* **2018**, *103*, 188-202.

[55] X. G. Wang, M. X. Huang, *J. Iron Steel Res. Int.* **2017**, *24*, 1073-1077.

[56] J. Han, A. K. da Silva, D. Ponge, D. Raabe, S. M. Lee, Y. K. Lee, S. I. Lee, B. Hwang, *Acta Mater.* **2017**, *122*, 199-206.

[57] H. Choi, S. Lee, J. Lee, F. Barlat, B. C. De Cooman, *Mater. Sci. Eng. A* **2017**, *687*, 200-210.

[58] A. S. Hamada, L. P. Karjalainen, M. C. Somani, *Mater. Sci. Eng. A* **2007**, *467*, 114-124.

[59] E. Bayraktar, F. A. Khalid, C. Levaillant, *J. Mater. Process Tech.* **2004**, *147*, 145-154.

[60] J. Lorthios, M. Mazière, X. Lemoine, P. Cugy, J. Besson, A. F. G. Lorenzon, *Int. J.Mech. Sci.* **2015**, *101*, 99-113.

[61] Z. C. Luo, M. X. Huang, *Steel Res. Int.* **2018**, doi.org/10.1002/srin.201700433.

Supplementary section

The supplementary Table 1 showed the tensile properties of high Mn steels which were achieved after processing via: (i) solution treatment and hot rolling followed by air cooling/water quenching or, (ii) solution treatment, hot rolling, cold rolling and annealing.

In the case of the first processing route, the single-phase face-centred cubic (fcc) austenite (γ) steels typically contained ~19-24Mn, 0.07-0.6C (in wt.% from here on), which transformed to body-centred cubic (bcc) α′-martensite + hexagonal closed packed (hcp) ε-martensite along with the formation of deformation-induced twins during tension and showed 600-1020 MPa ultimate tensile strengths (UTS) and 0.66-0.86 total elongation [1-3]. The UTS of an Fe-22Mn-0.6C steel was dominated by the formation of deformation twins [4]. Initially, dual-phase γ + ε-martensite steels contained ~15-20Mn and ~0.35-0.005C which transformed to α′ + ε-martensite upon tension showed 574-1234 MPa UTS. The latter range of UTS values for dual-phase steels was higher than that for single-phase γ steels [5-11]. In the case of Ref. [7], a dual-phase γ + ε-martensite microstructure obtained after solution treatment, water quenching and hot rolling transformed to ε-martensite during tension and resulted in a 842 MPa UTS. Alternatively, when the same steel was processed by solution treatment, liquid nitrogen quenching and hot rolling, the same dual phase microstructure transformed to α′ + ε-martensite on tension and recorded a higher UTS of 924 MPa [8]. Initially, multiphase steels with γ + ε + α′-martensite and/or bcc ferrite (α) phases were composed of ~9-19Mn, 2.4-3Al, ~3Si and transformed to α′ + ε-martensite during tension with 728-1437 MPa UTS. The latter value was higher than those of steels which contained originally single or dual-phase microstructures [10, 12-16].

In the case of further processing via cold rolling and annealing, a single-phase γ steel contained ~12-24Mn and 0.12-0.32C, transformed to α′ and/or ε-martensite during tension with 698-822 MPa UTS [17-20]. The dual-phase γ + ε-martensite/α steels with ~23-5Mn and 0.08-0.32C transformed to α′ + ε-martensite after tension with 696-1547 MPa UTS [19-26].

The multiphase steels with ~4-17Mn, ~0.06-0.1C compositions with primarily γ + ε + α′-martensite microstructures transformed to α′ + ε-martensite during tension with 856-1378 MPa UTS, which was higher than the UTS for similarly processed single and dual-phase steels [27-29]. Alternatively, other metastable multiphase steels with γ + ε + α′-martensite initial phases and carbides/carbonitrides within γ were composed of ~9-10Mn and recorded even higher 1193-1360 MPa UTS. The higher strength values were ascribed to a precipitation strengthening effect [12, 23].

Supplementary Table 1 Tensile properties of metastable Mn steels in literature.

Composition										Soln. HT			HR		Other	CR	Annealing			Other	Phases		LT(℃)	Speed(mm/min)	$\dot{\varepsilon}(s^{-1} \times 10^{-3})$	YS(MPa)	UTS(MPa)	e_u	e_f	Ref
Mn	Al	Si	Ni	Mo	Cr	V	Nb	C	N	T(℃)	t (h)	Med	T(℃)	R (%)		R(%)	T(℃)	t (h)	Med		Before	After							
23.8	2.7	3						0.6		1100	1	WQ		-							γ	α′+γ	RT	1.5	1	339	666	~0.67	~0.8	[1]
23.3	1.9	2.1					0.017		0.008	1230	1		1150								γ	α′+ε+γ	-75	-	1	220	800	0.72	0.86	[2]
19.1	1.8				4.4			0.07		1200	0.5		1200	88			1000	1	WQ		γ	γ+ε+α′	-273	0.42	0.14	195	1020	-	0.68	[3]
19.1	1.8				4.4			0.07		1200	0.5		1200	88			1000	1	WQ		γ	α′+ε+γ	RT	0.42	0.14	160	600	-	0.66	[3]
20.1	2.9	2.8													S(77%)		1000	2	WQ		γ+ε	α′+γ+ε	RT	-	0.1	289	764/1365‡	0.58	-	[10]
20	3	3								1000	2				S(77%)						γ+ε	α′+γ+ε	100	-	1	184	574	0.68	0.78	[5]
20	3	3								1000	2				S(77%)						γ+ε	α′+γ+ε	22	-	1	268	~600	0.73	0.85	[5]
20	3	3								1000	2				S(77%)						γ+ε	α′+γ+ε	-200	-	1	393	1234	0.45	0.5	[5]
17.8		5.2						0.35		1100	0.67				F						γ+ε	γ+ε+α′		2	0.667	425	918/1111‡	0.21/0.19‡	-	[6]
17								0.3		1000	1	WQ	1000								γ+ε	ε+γ	100	-	0.170	259	842	0.71	-	[7]
17								0.3		1000	1	WQ	1000								γ+ε	ε+γ	RT	-	0.170	180	730	0.11	-	[7]
17								0.3		1000	1	WQ	1000								γ+ε	ε+γ	0	-	0.170	197	720	0.06	-	[7]
17								0.3		1000	1	LNQ	1000								γ+ε	α′+ε+γ	100	-	0.170	381	924	-	0.21	[8]
17								0.3		1000	1	LNQ	1000								γ+ε	α′+ε+γ	RT	-	0.170	236	752	-	0.13	[8]
17								0.02		1150	2		1150	55							γ+ε	ε+γ+α′	-273	0.8	1	558	1073	0.65	0.75	[9]
17								0.02		1150	2		1150	55							γ+ε	ε+γ+α′	RT	0.8	1	343	691	0.25	0.26	[9]
15		0.02						0.005		1200	2		1150				900	5	WQ		γ+ε	α′+γ+ε	RT	3	1.25	~450	~773	0.35	0.39	[11]
18.8	2.9	2.9						0.04		1150	2		1150	91	F		1100	1	WQ		γ+α′+ε	α′+γ+ε	RT	-	1	420	829/1300‡	0.57/0.45‡	-	[13]
15.3	2.4	2.9						0.07	0.002	1100	2	AC	900	80			900	0.167	WQ		ε+γ+α′	α′	RT	0.6	0.2	332	1165	0.33	0.35	[14]
12													1100	83							γ+ε+α′	α′+ε+γ	RT	7.5	10	309	943/1032‡	0.09/0.09‡	0.21	[15]
12													1100	83							γ+ε+α′	α′+ε+γ	-150	7.5	10	548	1237/1395‡	0.13/0.12‡	0.22	[15]
12													1100	83							γ+ε+α′	α′+ε+γ	-196	7.5	10	676	1437/1704‡	0.19/0.17‡	0.25	[15]
19.6	3.1	2.9								1100	24		1200	70			900	1			γ+α+α′	α+α′+γ+ε	RT	-	-	397	781/1177‡	0.5/0.41‡	-	[16]
19.6	3.1	2.9								1100	24		1200	70			1000	1			γ+α+α′	α+α′+γ+ε	RT	-	-	336	728/1166‡	0.6/0.47‡	-	[16]
16	3	2.8								1100	24		1200	70			900	1			γ+α+α′	α+α′+γ+ε	RT	-	-	595	994/1303‡	0.31/0.27‡	-	[16]
16	3	2.8								1100	24		1200	70			1000	1			γ+α+α′	α+α′+γ+ε	RT	-	-	558	963/1301‡	0.35/0.3‡	-	[16]
9								0.05		1200	2		900				620	0.167			γ+α+Fe_3C	γ+α+α′+Fe_3C	RT	0.15	1	830	1034	~0.18	0.27	[12]
15.8	3	2.9													S(77%)		1000	2	WQ		γ+α+α′+ε	α+α′+ γ+ε	RT	-	0.1	406	1073/1585‡	0.48/0.39‡	-	[10]
24.1					0.008			0.12	0.02	1200	24		1150			33	1000	0.5	AC		γ	γ+ε	42	0.9	1	168	772/1175‡	0.42‡	-	[17]
22	3	3											1100			50	900	0.5			γ	γ+ε	-	-	0.4	290	698/1199‡	0.54‡	-	[18]
16.8	1.5	0.03						0.32		1150	5		1150	96		50	600	0.033			γ	-	RT	1.8	1	434	822	0.48	0.54	[19]
12	3							0.3					-			50	750	0.167			γ	γ+α′	RT	1.5	1	429	785	0.28	-	[20]
23.4	0.3	0.06						0.08		1150	5		1150	96		50	350	0.033		5%†	γ+ε	-	RT	1.8	1	254	844	0.276	0.28	[19]
23.4	0.3	0.06						0.08		1150	5		1150	96		50	550	0.083		5%†	γ+ε	-	RT	1.8	1	220	875	0.326	0.33	[19]
23.4	0.3	0.06						0.08		1150	5		1150	96		50	800	1			γ+ε	-	RT	1.8	1	279	792	0.205	0.21	[19]
23.4	0.3	0.06						0.08		1150	5		1150	96		50	800	1		5%†	γ+ε	-	RT	1.8	1	496	869	0.22	0.22	[19]
16.8	1.5	0.03						0.32		1150	5		1150	96		50					γ+ε	-	RT	1.8	1	1278	1547	0.014	0.03	[19]
16.8	1.5	0.03						0.32		1150	5		1150	96		50	350	0.033			γ+ε	-	RT	1.8	1	1249	1541	0.014	0.03	[19]
16.8	1.5	0.03						0.32		1150	5		1150	96		50	550	0.033			γ+ε	-	RT	1.8	1	1140	1331	0.022	0.07	[19]
16					4			0.1								20	700	0.0028			γ+ε	-	RT	1.5	1	780	1190	-	0.42	[21]
16					4			0.1								35	700	0.28			γ+ε	-	RT	1.5	1	890	1340	-	0.41	[21]
16					4			0.1								50	700	0.28			γ+ε	-	RT	1.5	1	970	1380	-	0.37	[21]
15.9					3.9			0.09					900			17	700	0.283	LNQ		γ+ε	α′+γ+ε	-	-	1	543	1222/1700‡	0.33‡	-	[22]
10.6		0.36		0.28				0.08	0.003	1200	1		1200			50	610	0.133	WQ		γ+α	α′+ε+γ+α		1.5	1	1080	1390	-	0.27	[23]
10	3	2						0.3					1200			50	800				γ+α	α′+α+γ	-	-	1	862	1128	0.63	0.64	[24]
6.1	2.2	1.6				0.23		0.29		-							810	0.167	WQ		γ+α	α′+α+γ		-	1	711	1530	0.19	0.2	[25]
5								0.1					-			70	650	18	AC		γ+α	α′+α+γ	RT	-	0.250	410	696	-	~0.4	[26]
10.6		0.36		0.28				0.08		1200	1		1200			50	550	2	WQ		γ+α+ $V_4(C,N)_3$	α′+ε+ γ+α +$V_4(C,N)_3$	-	1.5	1	1240	1360	-	0.09	[23]
9	0.08	0.3						0.05		1200	2		900			60	620	0.167			γ+α+Fe_3C	α′+α+γ+Fe_3C	RT	0.15	0.1	1060	1193	~0.23	~0.3	[12]

17	3	2	1					0.06		1100	2		1070	50		45					α′+ε+γ	-	RT	-	1	1200	-	0.01	0.02	[27]
17	3	2	1					0.06		1100	2		1070	50		45	700	0.083			γ+ε+α′	-	RT	-	1	650	920	0.35	0.42	[27]
17	3	2	1					0.06		1100	2		1100	52		42					γ+ε+α′	γ+ε+α′	RT	2.1	1	1080	1135/1157‡	0.02/0.02‡	0.05	*
17	3	2	1					0.06		1100	2		1100	52		42	500	0.083			γ+α′	γ+α′	RT	2.1	1	1075	1150/1173‡	0.02/0.02‡	0.42	*
17	3	2	1					0.06		1100	2		1100	52		42	625	0.083			γ+ε+α′	α′+ε+γ	RT	2.1	1	810	1006/1237‡	0.26/0.23‡	0.02	*
17	3	2	1					0.06		1100	2		1100	52		42	700	0.083			γ+ε+α′	α′+ε+γ	RT	2.1	1	465	856/1121‡	0.36/0.31‡	0.25	*
13								0.1					-			67	580	0.167			γ+ε+α′	-	-	2	-	1231	1257	0.17	0.33	[28]
13								0.1					-			67	600	0.167			γ+ε+α′	-	-	2	-	1007	1296	0.2	0.21	[28]
13								0.1					-			67	620	0.167			γ+ε+α′	-	-	2	-	561	1321	0.24	0.3	[28]
13								0.1					-			67	640	0.167			γ+ε+α′	-	-	2	-	484	1378	0.23	0.26	[28]
4.6		0.003						0.092					1200			70	670	1	AC		α+γ+α′	α+α′+γ	-	24	8	-	950	~0.16	0.18	[29]
4.6		0.003						0.092					1200			70	670	2	AC		α+γ+α′	α+α′+γ	-	24	8	-	951	~0.18	0.21	[29]
4.6		0.003						0.092					1200			70	670	4	AC		α+γ+α′	α+α′+γ	-	24	8	-	933	~0.16	0.19	[29]
4.6		0.003						0.092					1200			70	670	5	AC		α+γ+α′	α+α′+γ	-	24	8	-	959	~0.16	~0.2	[29]
4.6		0.003						0.092					1200			70	670	7	AC		α+γ+α′	α+α′+γ	-	24	8	-	868	0.21	~0.3	[29]
4.6		0.003						0.092					1200			70	670	8	AC		α+γ+α′	α+α′+γ	-	24	8	-	977	0.13	0.14	[29]
4.6		0.003						0.092					1200			70	670	9	AC		α+γ+α′	α+α′+γ	-	24	8	-	961	0.14	0.16	[29]
4.6		0.003						0.092					1200			70	670	10	AC		α+γ+α′	α+α′+γ	-	24	8	-	950	0.13	0.14	[29]

Legend: Soln. HT = solution heat treatment, T = temperature, Med= medium, AC= air cooling, WQ= water quenching, LNQ= liquid nitrogen quenching, HR =hot rolling, CR =cold rolling, R = reduction, γ = austenite, ε = epsilon martensite, α′ = alpha martensite, LT = loading temperature, $\dot{\varepsilon}$ = initial strain rate, YS= yield stress , UTS= ultimate tensile strength (engg), e_u = uniform elongation, e_f = total elongation, ‡= true stress/strain, * = present work, †=tension. The order of phases are in their decreasing amount of volume fraction.

References

[1] D. Hua, T. Zheng-You, L. Wei, W. Mei, S. Dan, *J. Iron Steel Res. Int.* **2006**, *13*, 66-70.

[2] B. X. Huang, X. D. Wang, Y. H. Rong, L. Wang, L. Jin, *Mater. Sci. Eng. A* **2006**, *438*, 306-311.

[3] K. Sato, M. Ichinose, Y. Hirotsu, Y. Inoue, *ISIJ Int.* **1989**, *29*, 868-877.

[4] I. Gutierrez-Urrutia, S. Zaefferer, D. Raabe, *Mater. Sci. Eng. A* **2010**, *527*, 3552-3560.

[5] O. Grässel, L. Krüger, G. Frommeyer, L. W. Meyer, *Int. J. Plasticity* **2000**, *16*, 1391-1409.

[6] Y. H. Wen, H. B. Peng, H. T. Si, R. L. Xiong, D. Raabe, *Mater. Design* **2014**, *55*, 798-804.

[7] M. Koyama, T. Sawaguchi, K. Tsuzaki, *Metall. Trans. A* **2012**, *43*, 4063-4074.

[8] M. Koyama, T. Sawaguchi, K. Tsuzaki, *Mater. Sci. Eng. A* **2012**, *556*, 331-336.

[9] K. H. Kwon, J. S. Jeong, J.-K. Choi, Y. M. Koo, Y. Tomota, N. J. Kim, *Met. Mater. Int.* **2012**, *18*, 751-755.

[10] G. Frommeyer, U. Brüx, P. Neumann, *ISIJ Int.* **2003**, *43*, 438-446.

[11] J. Chen, W.-n. Zhang, Z.-y. Liu, G.-d. Wang, *Mater. Sci. Eng. A* **2017**, *698*, 198-205.

[12] J. Han, S.-J. Lee, J.-G. Jung, Y.-K. Lee, *Acta Mater.* **2014**, *78*, 369-377.

[13] H. Ding, H. Ding, D. Song, Z. Tang, P. Yang, *Mater. Sci. Eng. A* **2011**, *528*, 868-873.

[14] M. C. McGrath, D. C. Van Aken, N. Medvedeva, J. E. Medvedeva, *Metall. Trans. A* **2013**, *44*, 4634-4643.

[15] J. S. Kim, J. B. Jeon, J. E. Jung, K. K. Um, Y. W. Chang, *Met. Mater. Int.* **2014**, *20*, 41.

[16] A. Pétein, P. J. Jacques, *Steel Res. Int.* **2004**, *75*, 724-729.

[17] H. C. Choi, T. K. Ha, H. C. Shin, Y. W. Chang, *Scripta Mater.* **1999**, *40*, 1171-1177.

[18] D. T. Pierce, J. A. Jiménez, J. Bentley, D. Raabe, J. E. Wittig, *Acta Mater.* **2015**, *100*, 178-190.

[19] F. Berrenberg, C. Haase, L. A. Barrales-Mora, D. A. Molodov, *Mater. Sci. Eng. A* **2017**, *681*, 56-64.

[20] S. Lee, B. C. De Cooman, *Metall. Trans. A* **2015**, *46*, 1012-1018.

[21] P. Behjati, A. Kermanpur, L. P. Karjalainen, A. Järvenpää, M. Jaskari, H. S. Baghbadorani, A. Najafizadeh, A. Hamada, *Mater. Sci. Eng. A* **2016**, *650*, 119-128.

[22] P. Behjati, A. Kermanpur, A. Najafizadeh, H. S. Baghbadorani, J.-G. Jung, Y.-K. Lee, *Mater. Sci. Eng. A* **2014**, *614*, 232-237.

[23] H. W. Yen, S. W. Ooi, M. Eizadjou, A. Breen, C. Y. Huang, H. K. D. H. Bhadeshia, S. P. Ringer, *Acta Mater.* **2015**, *82*, 100-114.

[24] S. Lee, B. C. De Cooman, *Metall. Trans. A* **2014**, *45*, 709-716.

[25] B. C. De Cooman, S. J. Lee, S. Shin, E. J. Seo, J. G. Speer, *Metall. Trans. A* **2017**, *48*, 39-45.

[26] J. Hu, W. Cao, C. Wang, H. Dong, J. Li, *ISIJ Int.* **2014**, *54*, 1952-1957.

[27] D. P. Escobar, S. S. F. Dafé, D. B. Santos, *J. Mater. Res. Tech.* **2015**, *4*, 162-170.

[28] D. W. Suh, S. J. Park, C. H. Lee, S. J. Kim, *Metall. Trans. A* **2009**, *40*, 264-268.

[29] A. Arlazarov, M. Gouné, O. Bouaziz, A. Hazotte, G. Petitgand, P. Barges, *Mater. Sci. Eng. A* **2012**, *542*, 31-39.

Graphical abstract

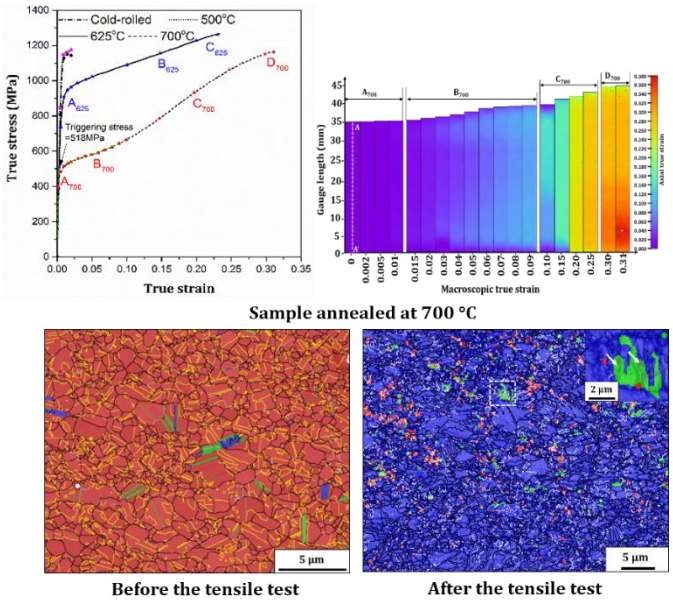

Digital image correlation depicted strain localisation during ε and α′-martensite formation upon uniaxial tension for the 625 and 700 °C samples. $\langle 111\rangle_{\gamma}$, $\langle 100\rangle_{\gamma}$ double-fibre, $\{hkil\}_{\varepsilon}$ and $\langle 110\rangle_{\alpha'}$ || ND fibres formation upon uniaxial tension was noted. Mixed mode and ductile fracture for the cold-rolled and annealed samples respectively, was also observed.

Highlights

- DIC depicted strain localisation during ε and α′-martensite formation upon tension.
- Formation of $\langle 111 \rangle_{\gamma}$, $\langle 100 \rangle_{\gamma}$ double-fibre, $\{hkil\}_{\varepsilon}$ and $\langle 110 \rangle_{\alpha'}$ || ND fibres upon tension.
- Mixed mode and ductile fracture for the cold-rolled and annealed samples, respectively.